polymers

Article

Induction Heating of Laminated Composite Structures with Magnetically Responsive Nanocomposite Interlayers for Debonding-on-Demand applications

Eleni Gkartzou[1], Konstantinos Zafeiris[1], Christos Tsirogiannis[1], Alberto Pedreira[2], Adrián Rodríguez[2], Pablo Romero-Rodriguez[2], Giorgos P. Gakis[1], Tatjana Kosanic-Milickovic[1], Apostolos Kyritsis[3] and Costas A. Charitidis [1,*]

[1] Research Lab of Advanced, Composite, Nano-Materials and Nanotechnology (R-NanoLab), School of Chemical Engineering, National Technical University of Athens, 9 Heroon Polytechniou, GR-15780, Greece
[2] AIMEN Technology Center, O Porriño, Spain
[3] Dielectrics Group, Physics Department, School of Applied Mathematical and Physics Science, National Technical University of Athens, 9 Heroon Polytechniou, GR-15780, Greece
* Correspondence: charitidis@chemeng.ntua;

Abstract: In the present study, the feasibility to achieve localized induction heating and debonding of multi-material composite structures is assessed in testing coupons prepared by Automated Fiber Placement (AFP) and extrusion-based Additive Manufacturing (AM) technologies. Nano-compounds of Polyether-ketone-ketone (PEKK) with iron oxide nanoparticles acting as electromagnetic susceptors have been processed in a parallel co-rotating twin-screw extruder to produce filament feedstock for extrusion-based AM. The integration of nanocomposite interlayers as discrete debonding zones (DZ) by AFP-AM manufacturing has been investigated for two types of sandwich-structured laminate composites, i.e., laminate-DZ-laminate panels and laminate-DZ-AM gyroid structures. Specimens were exposed to an alternating magnetic field generated by a radio frequency generator and a flat spiral copper induction coil, and induction heating parameters (frequency, power, heating time, sample standoff distance from coil) have been investigated in correlation with real-time thermal imaging to define the debonding process window without compromising laminate quality. Further insight on PEKK nanocomposites debonding performance was provided by thermal, morphological characterization and non-destructive inspection via X-ray micro-computed tomography at different processing stages. The developed framework aims to contribute to the development of rapid, on-demand joining, repair and disassembly technologies for thermoplastic composites, towards more efficient Maintenance, Repair and Overhaul operations in aviation sector and beyond.

Keywords: induction heating; debonding on demand; magnetic nanoparticles; 3D printing; Additive Manufacturing; CFRP; PAEK; disassembly; magnetically responsive; nanocomposite

Citation: To be added by editorial staff during production.

Academic Editor: Firstname Lastname

Received: date
Revised: date
Accepted: date
Published: date

1. Introduction

Thermoplastic (TP) composites are becoming increasingly popular in aviation sector and constantly expanding their range of use for both primary and secondary structures, exhibiting high damage tolerance, ease of formability, production efficiency, cost-effectiveness, lenient storage conditions, long shelf life and recyclability [1]. Automated composite manufacturing technologies employing high-performance TP polymers, namely of polyaryl ether ketones (PAEK) group of polymers (PEEK, PEKK, Low Melt-PAEK), PPS (polyphenylene sulfide) and PEI (polyetherimide), enable strong bonding, flexibility in design, homogeneous stress distribution, repair and reprocessing potential, and fatigue resistance [2]. These benefits are crucial in designing high-performance components that are lightweight and meet stringent safety and sustainability requirements in the aerospace industry, in compliance with industrial guidelines and regulations, to ensure safe and reliable aerospace components are manufactured and executed to the highest standard.

As more TP composite structures are manufactured, robust joining strategies need to be developed to ensure parts can be assembled efficiently at scale. The welding capability of TP materials allows to create seamless and reliable connections between components, eliminating the need for additional fasteners. Polymer and polymer composite welding is characterized by heating of joining parts above their respective glass transition (amorphous polymer) or melting (semi-crystalline polymer) temperatures and bringing them into intimate contact, promoting the diffusion of polymer chains across the interface and allowing the joint to cool down until reconsolidation is reached [3]. Depending on the heat generation mechanisms that act on the bonding interface, fusion bonding techniques may be classified as thermal, friction, and electromagnetic welding. Since polymers are generally poor heat conductors, external heating processes such as infrared radiation are typically slow, creating a large heat-affected zone and having limited value for welding hard-to-access locations and complex structures [4, 5]. Therefore, internal heat generation mechanisms, such as resistance, induction, and ultrasonic welding, have been extensively investigated for joining and repair of TP parts. The aerospace industry already employs welding as an assembly method for parts made of TP composites, with the assembly of the leading edges of the wings of the Airbus A340-600 and A380 by resistance welding, and induction welding applied on the empennage of the Gulfstream G650 being notable examples, resulting in significant process advancement and extensive certification programs with full-scale component tests [6]. In parallel, the development of new techniques and processes for easy recycle and repair of bonded structures is becoming of great interest for the industry, with a growing need to develop adhesives and joining methods that maintain their adhesion strength during service life but can be easily dismantled upon application of external stimuli for repair, reuse, or recycling [7].

Induction heating (IH) is a non-contact, energy-efficient process to generate localized heat with precise temperature control, speed, reproducibility, and adaptability to complex geometries. IH relies on heating of electromagnetic and conductive materials (susceptors) placed within an alternating electromagnetic field operating in the kHz to MHz frequency range [8]. A typical IH system consists of a radio frequency (RF) power generator connected to an external circuit for impedance matching and a set of capacitors connected in parallel to an induction coil, allowing to reach the targeted resonance frequency. Depending on the operation, a magnetically inert apparatus where the workpiece is positioned in static or relative motion mode is also employed. An alternating voltage is applied to the induction coil, resulting in an alternating current flow in the coil circuit which produces a time-variable magnetic field in its surroundings. Energy is transferred to the workpiece, with heat generation taking place as the loss of energy due to electromagnetic dissipation phenomena. For heating applications on composites, three induction coil types are commonly employed, i.e., single turn, solenoid and flat spiral/pancake coils, however coil geometry and size may be designed according to specific geometry constraints of the workpieces under processing. The magnetic field intensity distribution is influenced by power, frequency, coil geometry and coil-to-workpiece electromagnetic coupling (i.e., standoff distance from the workpiece surface), thus the combined effect of these factors should be investigated to define an optimum processing window [9, 10]. As heating rate is estimated to be proportional to the square of the power supply frequency and increases quadratically by increasing generator power and reducing coil standoff distance, a tradeoff should be achieved to promote internal heat conduction and temperature uniformity in the workpiece, as high power density values above a certain threshold could result in overheating and material degradation, as well as introduce undesirable temperature gradients in materials with low thermal conductivity [9].

The main dissipation phenomena which can be exploited by different susceptor material types include Joule heating due to eddy currents occurring in electrically conductive materials, hysteresis heating and relaxation losses [11]. The heating process has a well-defined critical point where susceptor materials reach a limit temperature (Curie temperature), marking a transition to a paramagnetic state. For temperatures below the Curie point, the primary mechanism of heat generation in electrically conductive materials is associated with resistive heating generated by macroscopic eddy currents according to the Joule effect, which has a greater impact over all heat generation mechanisms. The second mechanism of heat generation due to magnetic hysteresis losses occurs in ferro/ferrimagnetic materials in multi-domain magnetic state, where the reversal of the magnetization direction takes place via magnetic domain wall displacement and a small amount of energy is dissipated into heat during each magnetic polarization-depolarization cycle (hysteresis loop) [12]. The hysteresis loop is characterized by three material-dependent parameters, i.e., saturation magnetization, remanent magnetization (remanence), and coercivity. As magnetic hysteresis is a non-equilibrium process, the theoretical maximum amount of heating power is rarely realized due to the occurrence of relaxation processes, i.e., in the absence of an external field the macroscopic remanent magnetization tends to reduce due to activation by thermal energy of internal spin switching (Néel relaxation) or particle physical rotation (Brownian relaxation) if the surrounding medium has sufficiently low viscosity [13]. In the case of particulate susceptors below a critical particle size (superparamagnetic limit), the multi-domain state becomes energetically unfavorable, and each particle represents a single magnetic domain with superparamagnetic behavior, exhibiting strong magnetization along the direction of the external magnetic field. However, the reduced particle volume and associated decrease of the energy barrier against magnetization reversal act in favor of relaxation losses [14]. In addition, the degree of agglomeration has also been found to induce weak dipole–dipole interactions, leading to agglomerates behaving like particles with larger effective volume, showing hysteretic heating behavior, with increased coercivity and heating power [15]. In this context, only certain combinations of particle size, size distribution as well as external field frequency and amplitude may fully exploit the heating potential of particulate magnetic susceptors. In principle, field frequency of several hundred kHz in combination with low field amplitude (few kA/m) may be applied for superparamagnetic particles, while a higher field amplitude (a few tens of kA/m) and lower frequency (few hundred kHz) are suitable for particles with hysteretic behavior [13].

Unlike metals, neat polymers and composites do not typically possess the inherent electromagnetic properties for inductive heating, thus susceptors need to be introduced for the conversion of electromagnetic field energy into heat. Polymer systems with magnetic fillers relying on hysteresis losses for heat generation are considered promising for attaining uniform and efficient heating at lower concentrations [16]. The capability of magnetic nanoparticles to dissipate energy in an alternating magnetic field is frequently reported as Specific Absorption Rate (SAR, i.e., the amount of heat generated per mass unit of magnetic material and per unit time) [17]. The ability of magnetic nanoparticles to act as heat mediators is affected by several intrinsic and extrinsic factors, including their shape, size and chemical composition, agglomeration state, magnetic anisotropy, temperature, as well as external magnetic field intensity and frequency [18]. Additionally, by selecting magnetic particles with a Curie temperature above the polymer melting temperature range and safely below the thermal degradation onset, a self-regulating heating process can be achieved for controlled heating applications [19, 20].

Various types of magnetic particles, including iron and iron oxide-containing ferrites, nickel and cobalt-nickel alloys have been investigated as powder additives to provide inductive heating functionality, with recent studies further contributing to the fundamental understanding of their unique micro-/nanoscale magnetic properties [21,22,23]. To improve the inductive heating characteristics of magnetic nanostructures, many approaches have been taken to investigate SAR correlation with particle size, composition, shape, inter-particle interaction and inter-phase exchange coupling, while synthetic strategies have been proposed to obtain engineered nanoparticles with precise control over their magnetic properties [21]. In polymer systems, several studies have presented new susceptor configurations with embedded magnetic micro-/nanoparticles, with special focus on the development of film susceptors for structural adhesive joints. The induction heating behaviour of thermoplastic polyurethane (TPU) adhesive film with embedded Fe_3O_4 nano-/microparticles (0.27, 2, and 9 μm average size) was examined by Bae et al., employing a four-turn helical coil (300 mm inner diameter) and applied input power of the induction heater varying from 2 to 5 kW at 750 kHz frequency [24]. The effect of Fe_3O_4 particle size, particle concentration, susceptor film thickness and power were assessed in terms of initial heating rate and maximum temperature attained, with heating rates up to 3.1 °C/s and maximum temperature up to 324.5 ^{0}C (t=500 s) achieved. The amount of heat generation was found to be proportional to the content of Fe_3O_4 particles, film thickness, and input power, while an inverse effect was demonstrated with the increase of Fe_3O_4 particle size, with nanometer-sized particles found to be more efficient for achieving higher temperatures. In a similar study by the same research group, TPU susceptors with iron particles (average diameter of 8, 43 and 74 μm) were also assessed, under similar conditions, with composites consisting of larger iron particles demonstrating a higher heating rate (up to 2.7 °C/s for 20 wt% Fe) in all compositions tested [25]. On the contrary, in a study conducted by Baek et al., the maximum temperature reached (200 ^{0}C or higher within t=10 s) did not present significant dependency to Fe_3O_4 weight ratio for film susceptors (450 μm thickness), prepared by mixing polyamide 6 and Fe_3O_4 nanoparticles (average size: 200 nm), investigated at different weight ratios (50, 67, 75, and 80 wt% of Fe_3O_4), employing a multi-turn induction coil (15 mm inner diameter) and induction heating parameters of 3.4 kW power output, 100 kHz frequency and 45 A output current [26]. In a recent study by Raczka et al., the influence of different agglomeration states among magnetite nanoparticles (dispersed, micrometer-assemblies, hard agglomerated) incorporated in polydimethylsiloxane (PDMS) matrix was investigated in terms of inductive heating performance of the composites [14]. For a field amplitude above the coercivity threshold, a larger hysteresis surface area and increased heating rate were attained for composites with dispersed nanoparticles compared to other agglomeration states, while an identical heating performance was recorded at lower field amplitudes. This effect was attributed to the possible contribution of additional force of neighboring nanoparticles in magnetic moment relaxation mechanisms, also indicated by a decrease of coercivity and remanence in agglomerated states. Particles of iron, nickel, and magnetite were evaluated as susceptor materials in polypropylene (PP) and polyetheretherketone (PEEK) matrices by Martin et al., complemented with an analytical model for the prediction of heating capacity of ferromagnetic particles [16]. Susceptor samples were prepared by melt mixing magnetic particles with either PP or PEEK at 5 and 10% vol. compositions and tested under a 32 kAm^{-1} magnetic field amplitude and a frequency of 269 kHz. Fe_3O_4 was found to be more suitable for PEEK heating, with 10% vol. PEEK/Fe_3O_4 sample exhibiting temperature increase above 400 ^{0}C after 45 s, while a moderate heating efficiency was recorded for 5% vol. PEEK/Fe_3O_4 sample, which reached a plateau temperature of 283 ^{0}C, in equilibrium with thermal losses in the surrounding media. Cheng et al. investigated the induction heating performance and adhesive strength after repeated debonding/rebonding cycles of poly(ethylene-methacrylic acid) (EMAA) adhesives with different mass loading (5, 20, and 30 wt%) of Fe_3O_4 nanoparticles (50-100 nm diameter), tested under varying intensities of magnetic flux up to 0.07 T at 189 kHz operating frequency [27]. Nanocomposite adhesives with 5 wt% Fe_3O_4 were found to be effective in retaining 100% of the original bond strength for up to five cycles of repeated debonding and rebonding, measured using a tensile lap-shear test. Analytical and computational models using a hysteresis loss theory were also developed to characterize the effects of key design parameters (Fe_3O_4 mass loading and magnetic flux) on the heating performance, with good agreement with experimental results. A limited number of thermoplastic compounds with particulate electromagnetic susceptor fillers have been commercialized, with the most notable example being the proprietary thermoplastic compounds developed by Emabond Solutions, USA, available in several formats (extruded profiles, injection molded gaskets, AM feedstock) that can generally be applied as additional materials in the weld zone for the formation of tongue-in-groove type of shear joints or custom joint configurations [19].

Material extrusion AM is one of the most popular AM processes that is particularly versatile regarding material compatibility and multi-material integration, spanning different polymer types and functionalities. Additive Manufacturing enables local control over material properties and this, if coupled with multi-material integration, can be used to create joints with tailored physical and mechanical adhesive properties, opening the possibility to explore new joint design strategies. Tailoring additively manufactured adherends and adhesives, following Design for AM principles has shown great promise, multiple investigations in the field of adhesives applied to AM components [28]. Recently, extrusion-based AM has been employed to embed circuits and heating elements for joining by the application of a controlled electric current [29]. Strategies for AM joining aim at maximizing joint performance, through functionally graded structures that modify the adherend geometry, as well as compositional variations to change material properties for a tunable adhesive stiffness [30]. In parallel, AM offers several advantages to apply Design-for-Disassembly principles to produce components that can be easily dismantled. Using a multi-material AM approach in combination with Thermally Expandable Microspheres, easily separable compounds have been achieved using heat as external trigger [31]. Magnetically active composites as raw materials for extrusion-based AM have been also assessed, demonstrating that coupling of filler loading with applied magnetic field frequency and intensity can be employed for proper control of heating capacity [32]. Yet additional research is required to enhance manufacturing reliability and repeatability and further expand to new material types and applications [28].

Considering the above, the aim of this study is to assess the feasibility of integration of discrete debonding zones (DZ) in multi-material composite structures, to achieve targeted thermal activation and separation of CFRP laminates for debonding-on-demand applications. To this end, a previously investigated nano-compound of Polyether-ketone-ketone (PEKK) with iron oxide nanoparticles has been processed to produce filament feedstock for extrusion-based AM [33]. An integrated manufacturing process sequence of AFP/AM was employed for the fabrication of sandwich-structured composite laminates with magnetically responsive interlayers, that were subsequently exposed to an alternating magnetic field to assess their induction heating performance and define the debonding process window without compromising laminate quality. Further insight on PEKK nanocomposites debonding performance was provided by thermal, morphological characterization and non-destructive inspection via X-ray micro-computed tomography at different processing stages. The developed framework is part of an innovative data-driven methodology to design, manufacture and maintain multi-functional and intelligent airframe parts through a cost-effective, flexible and multi-stage manufacturing system based on the combination of robotized AFP and Fused Filament Fabrication (FFF) technologies, developed in the framework of H2020 DOMMINIO project (G.A. No. 101007022) [34].

2. Materials and Methods

2.1 FFF nanocomposite feedstock preparation

The production of the nanocomposite filament was performed via compounding and filament extrusion process, by employing a co-rotating parallel twin screw extruder (Thermo Fisher Scientific Process 11, Karlsruhe, Germany) equipped with a gravimetric feeding system to introduce nanoparticles in powder form and a melt-pump coupled with the extruder setup to stabilize extrudate diameter for monofilament production. The take-up setup consisted of an air-cooling system (conveyor belt-based), a triaxial laser system (ODAC 13TRIO, Zumbach Electronic AG, Orpund, Switzerland) for real-time inspection of filament diameter and ovality, and a winding system operating with a synchronized spooling rate. The PEKK material employed in this study was a medium flow grade PEKK copolymer with 60/40 ratio of terephthaloyl to isophthaloyl moieties and low crystallization rate (KEPSTAN® 6002, Arkema, Europe). Iron oxide nanoparticles (Fe_3O_4) with average diameter of 20 nm with Polyvinylpyrrolidone (PVP) coating (1% content) and 99.5% purity were supplied by GetNanoMaterials, France. Before processing, feedstock materials were dried at 120 ^{0}C for 6 hours. The nanocomposite composition used in this study (7.5 wt.% content of Fe_3O_4 nanoparticles) was selected based on previous research, where a comparative assessment of different nanoparticle types and concentrations in PEKK matrix was conducted to assess induction heating efficiency in specimens produced by injection molding [33]. Extrusion conditions for nanocomposite filament production are presented in Table 1. Nanocomposite filament with 7.5 wt.% content of Fe_3O_4 nanoparticles was produced with average diameter of 1.79 ± 0.11 mm (Figure 1).

Table 1. Extrusion conditions filament production of PEKK nanocomposite with 7.5 wt.% content of Fe_3O_4 nanoparticles.

Zone	2	3	4	5	6	7	8	Die	Melt Pump	Screw Speed (rpm)	Melt Pump Speed (rpm)	Gravimetric Feeder Speed (rpm)
Set Temp. (^{o}C)	290	320	325	330	335	335	340	340	335	340	15	10

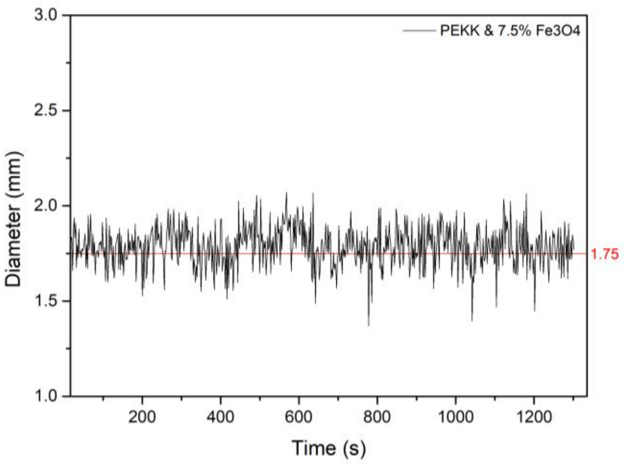

Figure 1. Filament diameter in-line measurement data obtained from USYS Data software for PEKK & 7.5% Fe_3O_4.

2.2 Additive Manufacturing of Sandwich Composite specimens

Robot-assisted AFP and FFF processes were employed for composite specimen manufacturing, through an integrated, multi-stage manufacturing workflow (Table 2). Two types of sandwich-structured composite laminate panels were prepared, i.e., Laminate-Debonding Zone-Laminate panels (Type I Specimens), consisting of two monolithic composite laminates manufactured by AFP and an FFF interlayer of nanocomposite filament with magnetic susceptors in the middle, as well as Laminate-Debonding Zone-FFF Gyroid (Type II Specimens), with an FFF gyroid structure (pure PEKK) 3D printed on top of the debonding zone.

Continuous fiber, monolithic composite laminates were manufactured by AFP employing high-performance LM-PAEK unidirectional (UD) prepreg tapes with 66% carbon fiber mass fraction (Cetex TC 1225, Toray Advanced Composites). The in-situ consolidated laminates were composed of unidirectional– layers, following a stacking sequence of [45/0/135/0/0/135/90/45/0/0/4/90/135/0/0/135/0/45] and [-45/45/0/0/90/90/45/-45]s for Type I and Type II specimens respectively. Optimum process parameters were defined to maximize interlayer adhesion and minimize the void content, namely a 6-kW diode laser was used to reach a nip point temperature of 400 °C, while applying 500 N compaction force, 250 mm/s layup speed and 220 °C mould temperature. After AFP manufacturing, the top surface of the composite laminate was heated by the laser source above LM-PAEK melting temperature to promote adhesion during FFF deposition of the nanocomposite filament with magnetic susceptors. The FFF process focused on obtaining the optimum quality parameters during deposition, using a 0.8 mm nozzle with a nominal layer height of 0.3 mm, extrusion width of 0.8 mm, 10 mm/s printing speed and nozzle temperature of 370 °C. In Type I specimens, a top composite laminate with the same stacking sequence as described above was manufactured by AFP over the nanocomposite layer. In Type II specimens, a gyroid lattice structure with unit cell size of 15 mm and a top solid layer was 3D printed via FFF using commercial PEKK filament (ThermaX™ PEKKKA, 3DXTECH, USA). Composite panels of 250 x 250 mm were subsequently cut with a water jet cutter to obtain testing coupons with equivalent active surface areas (2000 mm^2) for the assessment of induction heating efficiency.

Table 2. Type I & II sandwich-structured composite laminate specimen manufacturing

	Type I Specimens	Type II Specimens
Process sequence	AFP → FFF → AFP	AFP → FFF → FFF
Cross Section Schematic	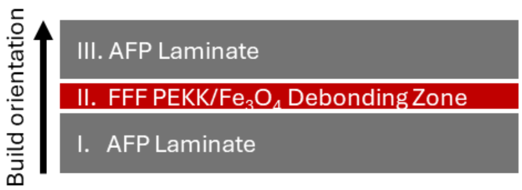	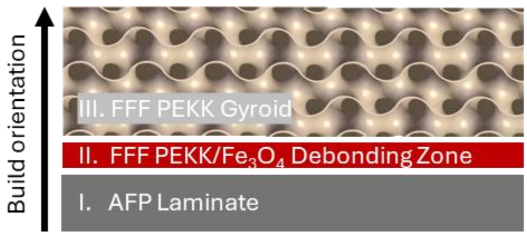
Cross Section image (scale bar: 2.5 mm)	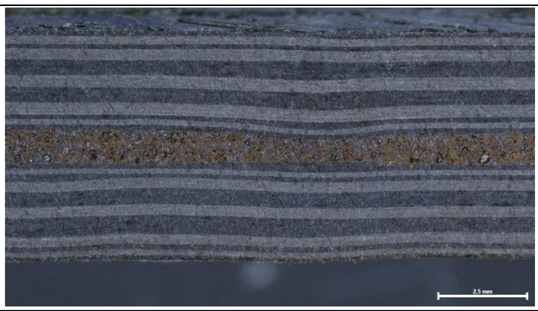	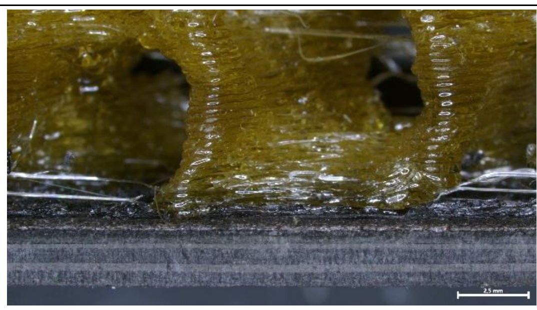
Design	AFP laminate stacking sequence: [45/0/135/0/0/135/90/45/0/0/45/90/135/0/0/135/0/45] Consolidated AFP laminate thickness: 2.7 mm FFF Debonding Zone thickness: 0.6 mm	AFP laminate stacking sequence: [-45/45/0/0/90/90/45/-45]$_s$ Consolidated AFP laminate thickness: 2.45 mm FFF Debonding Zone thickness: 0.6 mm FFF Gyroid lattice unit size: 15 mm
W x D x H	100 x 20 x 6 mm	80 x 25 x 18 mm

2.3 Characterization methods

2.3.1 Thermal Analysis

Differential Scanning Calorimetry (DSC) was employed to study the specimens' nanocomposite layer (PEKK & 7.5% Fe_3O_4 NPs) in three different stages of thermal processing, namely pellet form (Stage 1 – S1), FFF nanocomposite layer extracted from Type I specimens (Stage 2 – S2), and remelted nanocomposite after subjected to induction heating and extracted from the debonded specimens (Stage 3 – S3). The calorimetric measurements were performed employing a TA Q200 DSC apparatus (TA Instruments, USA), calibrated with sapphire for heat capacity and indium for temperature and enthalpy, on samples of ~6-9 mg in mass closed in TA standard aluminium pans. The specimens were initially heated at a rate of 10 ^{o}C/min from room temperature to 360 ^{o}C for 5 minutes. This temperature value was selected since it is above the PEKK equilibrium melting temperatures to erase the thermal history. Afterwards, specimens were cooled at a rate of 40^{o}C/min to room temperature, followed by a second heat scan at a rate of 10^{o}C/min up until 400 ^{o}C. The second heat scan enabled the measurement of the glass transition and melting temperatures, and the melting enthalpy for specimens obtained from the three processing stages (S1-S3). Thermogravimetric analysis was carried out with a NETZSCH/ STA 449 F5 Jupiter thermal analysis system under a synthetic air atmosphere from 25 ^{o}C to 900 ^{o}C and a heating rate of 10 ^{o}C/min, to investigate the thermal stability and the effect of thermal processing stages (S1-S3) at the onset of thermal degradation. To this end, the onset decomposition temperatures corresponding to 5% weight loss of the initial mass were calculated from each TGA thermogram, denoting the temperature at which thermal decomposition begins.

2.3.2 Scanning Electron Microscopy (SEM)

Surface analysis of debonded laminate specimens was performed using SEM coupled with Electron Diffraction Spectroscopy (EDS). SEM characterization was conducted in a Hitachi TM3030Plus SEM, to study the morphology of the nanocomposite layer (PEKK & 7.5% Fe_3O_4 NPs) and perform elemental analysis, following the debonding of the tested specimens. All specimens were sputter-coated with gold to effectively observe the morphological details of the debonded areas.

2.3.3 Micro-computed tomography (mCT)

Segments derived from nanocomposite FFF filament, Type I and II specimens were analyzed with micro-computed X-ray tomography with SkyScan 1272 High Resolution Micro-CT (Bruker microCT, Kontich, Belgium) for the assessment of nanoparticle degree of agglomeration and non-destructive inspection of Type I & II specimens. The obtained shadow angular projections were used for the reconstruction of the virtual slices through the sample. Raw data cross sections were generated using NRecon reconstruction software (v1.7.0.4 by Bruker microCT) by implementing the Feldkamp algorithm. The original grayscale slices were processed in CT-Analyser (v1.18.4 by Bruker microCT) to improve detail resolution (contrast enhancement) and proceed with particle isolation and segmentation. Reconstructed results were visualized as a set of orthogonal slices crossed at selected points of the reconstructed volume in DataViewer software (v1.2.5.7 by Bruker microCT). Morphological analysis in filament samples was conducted by sampling sub-volumes of interest of 5 mm^3 to reduce computation time.

2.4 Induction Heating and Thermal Imaging

2.4.1 Induction heating setup

Induction heating of Type I and II specimens was performed using a TruHeat HF 5010 unit (Trumpf Hüttinger, Germany) with max. 10kW power supply, generator current up to 35 A and frequency range of 50 kHz to 1000 kHz. The RF generator is connected to the external circuit, comprising of a 16:1 transformer (560 A current transformer output) and 4 x 0.33 μF capacitors, forming a series circuit together a flat spiral inductor made of two concentric ellipsoid turns, connected to the output. The application of an alternating voltage induces a periodic oscillation of current and voltage in the series circuit, where the frequency is automatically calculated by the generator to reach the LC resonance frequency of the induction coil. To investigate the induction heating capacity of the embedded Debonding Zones in Type I and Type II specimens, RF power supply values within the range of 2-3 kW were tested in conjunction with different coupling distances (standoff distance) between the induction coil and the workpiece, in the range of 20-45 mm. Induction heating process parameters are summarized in Table 3.

Table 3. Induction heating process parameters

Control Factor	Units	Levels					Response variables
Generator Power (P)	kW	2	2.25	2.5	2.75	3	▪ Heating Rate ▪ Time to reach debonding temperature >320 ^{0}C
Frequency	kHz	415	414	414	413	412	
Current (rms)	A	302	322	341	350	376	
Voltage	V	354	377	400	413	442	
Standoff Distance (D)	mm	20	25	35	40	45	

For specimen static heating and debonding trials, a bespoke mounting set up was designed and 3D printed (Figure 2 and Figure 3). The mounting setup consisted of a linear axis with a motorized lead screw actuator for specimen movement below the coil, a sliding base with modular subcomponents secured in place with 3 alignment pins to adjust the standoff distance and a ceramic blade mounting base consisting of two mirrored columns with sequential 1 mm slots for adjustment of blade height. Specimen temperature was recorded throughout the entire experiment with the use of a thermal imaging camera (FLIR C5, Teledyne FLIR LLC, USA).

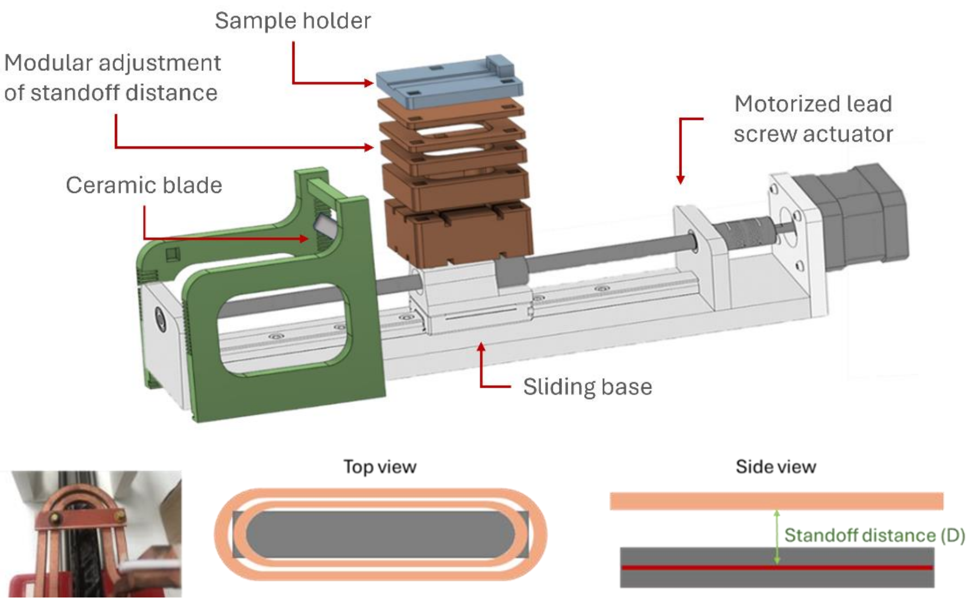

Figure 2. Schematic of the mounting set up for specimen static heating and debonding trials

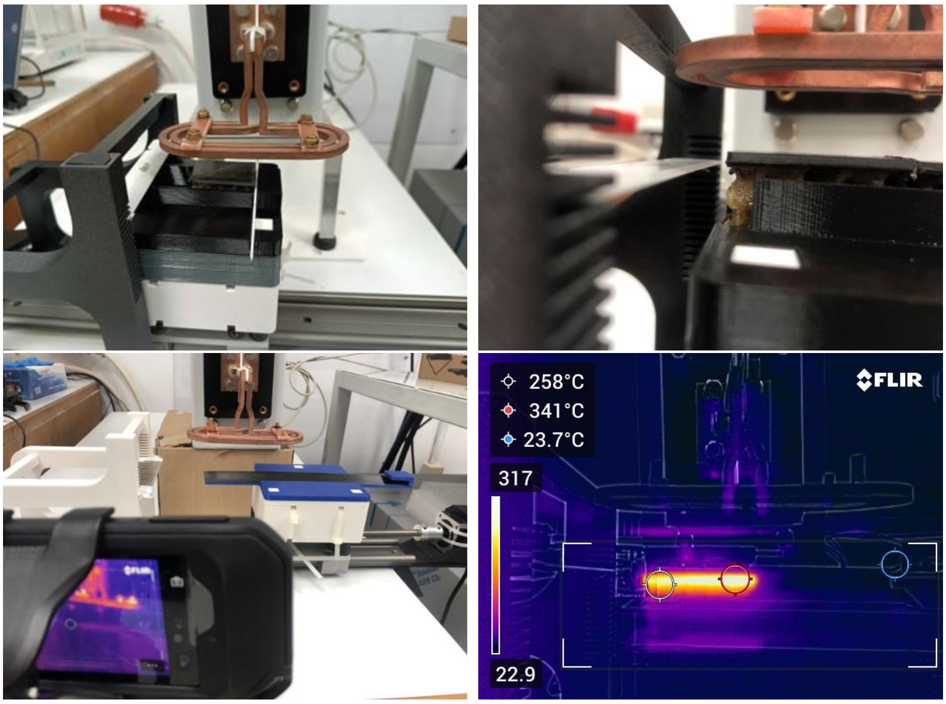

Figure 3. Induction heating testing setup

2.4.2 Induction Heating Simulation

A computational model was developed to simulate the induction magnetic field generated in the surroundings of the coil during the induction heating process. A computational domain was designed to simulate the induction heating setup, including the geometrical characteristics of the flat spiral/pancake coil and the dimensions of the workpieces (Figure 4). The pancake-ellipsoid coil was simulated by imposing the respective experimental conditions of Table 3. A computational mesh of 197247 elements was used to discretize the computational domain, and a quadratic basis function was employed for the dependent variables. The developed model is based on previous works, and the set of equations (as described in Appendix A) was solved using COMSOL Multiphysics software [35-37]. As in previous works, a bounding box around the experimental setup was selected to model the surrounding air, and a magnetic insulation boundary condition was imposed on the bounding box boundaries. The size of the bounding box size was determined by increasing the box size until the model results were unaffected by further size increase. Indicative simulation results for magnetic flux density norm and magnetic field intensity for 30 mm standoff distance are presented in Figure 5.

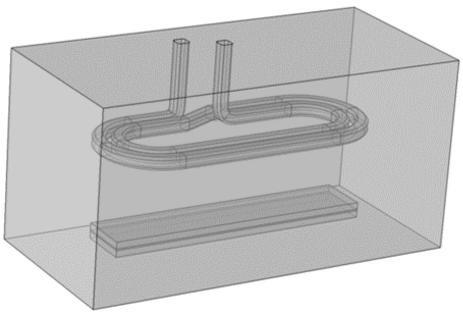

Figure 4. Simulated geometry for the induction heating model.

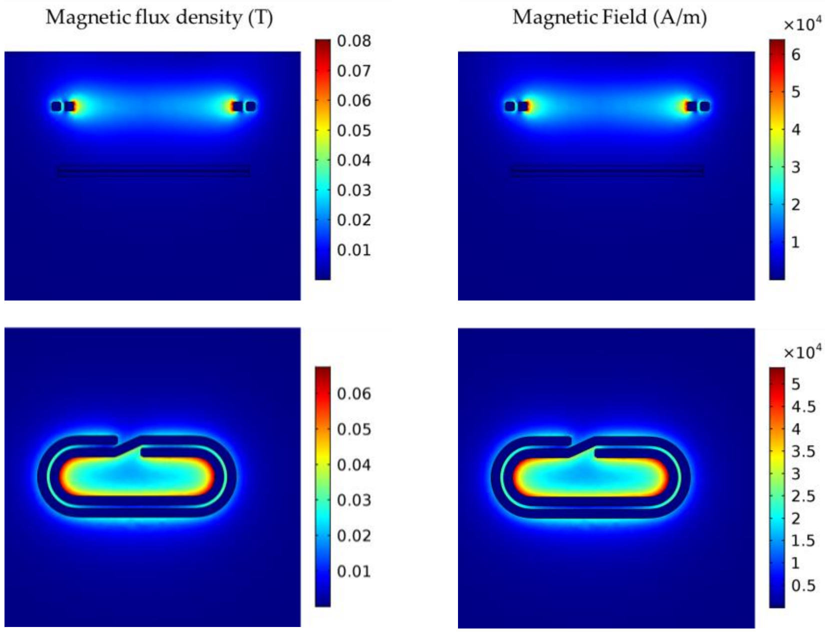

Figure 5. Simulation results for magnetic flux density norm and magnetic field intensity for 30 mm standoff distance

3. Results & Discussion

3.1 Filler dispersion analysis

Reconstructed results were initially visualized as a set of three orthogonal slices crossed at selected points of the reconstructed volume in DataViewer software (version 1.2.5.7 by Bruker microCT). Nanoparticle agglomerates in FFF filament are highlighted as high X-ray absorption areas (towards white in grayscale), while the surrounding polymer matrix is depicted in darker gray (Figure 6a). Ambient air surrounding the samples is depicted as black.

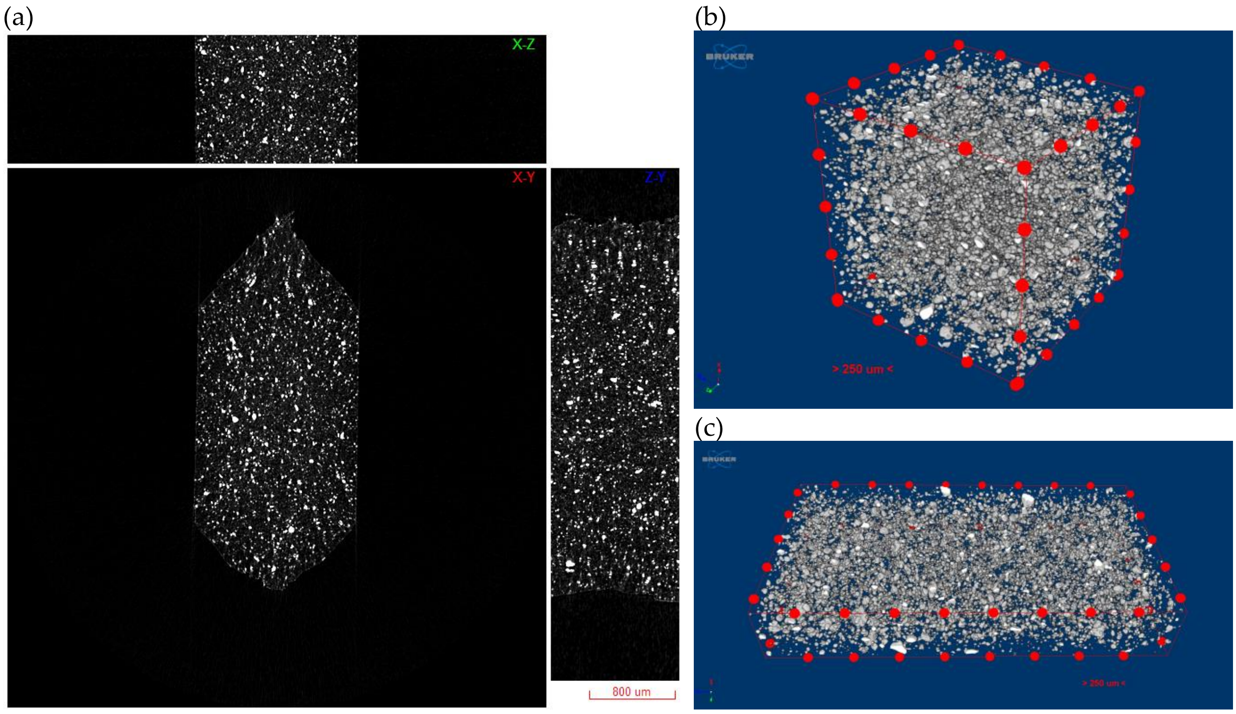

Figure 6. Indicative images of agglomerate distribution for PEKK 6002 + Fe3O4 7.5wt% FFF filament sample: a) XZ, XY, ZY cross sections of reconstructed grayscale slices (scale bar: 800um); b,c) 3D visualization of sample volume (scale bar: 250um, 2.5 μm voxel size).

Due to the high nanoparticle concentration and the inherent agglomeration tendency of magnetic nanoparticles, the mixing process during compounding was not able to eliminate agglomerated particles, as observed in Figure 6b & c. Nonetheless, an even dispersion of agglomerates was obtained that was further analyzed to assess agglomerate size distribution and average distances. To this end, agglomerated particles were labelled by colors corresponding to their size, grouped in size classes of 5 um range (namely 0-5 | 5-10 | … | >45 um), and the volume-equivalent sphere diameter model was employed for agglomerate size classification. The accuracy of this classification approach is considered sufficient, given the average sphericity values for all datasets investigated were above 0.84. The mean separation distance between each agglomerate and its nearest neighbor was also assessed by a 3D-construction process obtained through a Delaunay triangulation algorithm [38]. For this analysis, a custom python script was developed to post-process the list of centroid coordinates of each agglomerate particle, as extracted from the individual object analysis processed by CT-Analyser (v1.18.4 by Bruker microCT). Centroid coordinates were analyzed to identify agglomerate particles in close proximity (first neighbors) and subsequently build a 3D Delaunay triangulation mesh connecting the respective centroid points. The mesh edge lengths connecting first neighbors were subsequently calculated and plotted to derive the distribution of agglomerate separation distance. As observed in Figure 7, the majority of agglomerates (>88%) are below 20 um diameter range, with mean diameter of 12 ± 7 um. In addition, even distribution of agglomerates is confirmed from the calculated interparticle distances, that are centered around 50 um average distance (Figure 8).

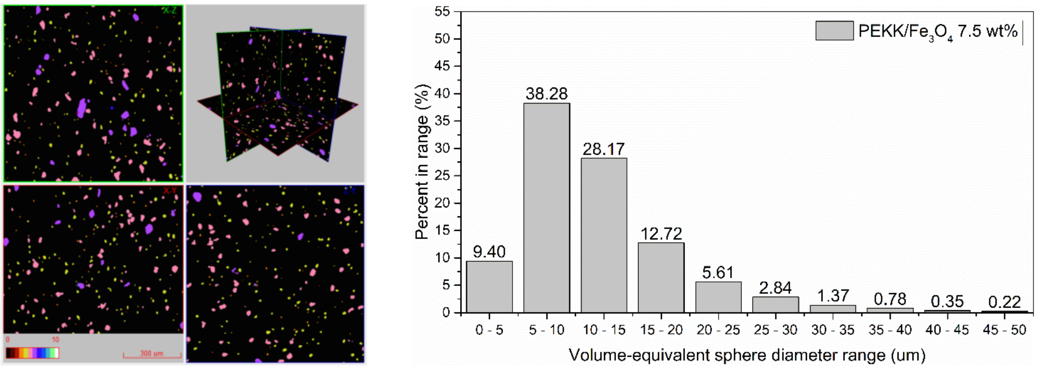

Figure 7. Left: Color-coded 2D visualization of agglomerate size (scale = 300 μm); Right: Agglomerate size classification employing the volume-equivalent sphere diameter model (PEKK 6002 + Fe_3O_4 7.5wt%).

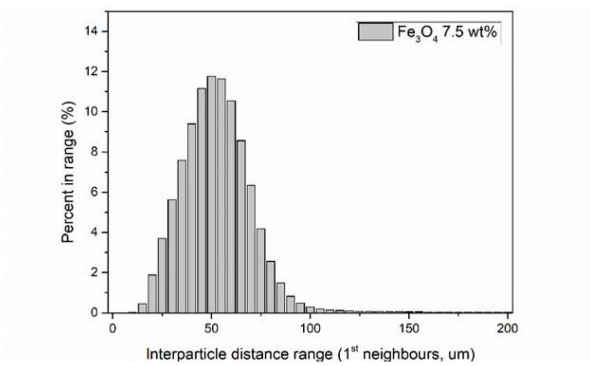

Figure 8. Distribution of agglomerate separation distances for PEKK 6002 + Fe_3O_4 7.5wt%.

3.2 Thermal Properties

TGA thermograms and calculated values of thermal degradation onset temperature (T_o) for each stage are presented in Figure ***9***. The results indicated the materials to be stable up to at least 500 °C without significant degradation. A small increase is observed for the onset of thermal degradation between the nanocomposite material in pellet form (T_o = 520.5 °C) and the subsequent processing stages (529.6 °C and 523.2 °C for FFF and re-melted material respectively). As reported in literature, PEKK matrices can evolve due to chemical transformation of the macromolecular chains, possibly attributed to crosslinking mechanisms initiated by scissions located in the carbonyl and ether bonds, creating radicals which miss hydrogen molecules. Radicals can then rearrange by removing hydrogen molecules from aromatics cycles forming phenyl radicals, which can then rearrange with an adjacent radical to produce crosslinks [39]. Another possibility for phenyl radical is to rearrange by internal combination, to produce dibenzofuran or fluorenone derivatives. In this context, the increase of thermal stability observed between S1 and S2 processing stages may be related to crosslinking mechanisms activated during FFF processing.

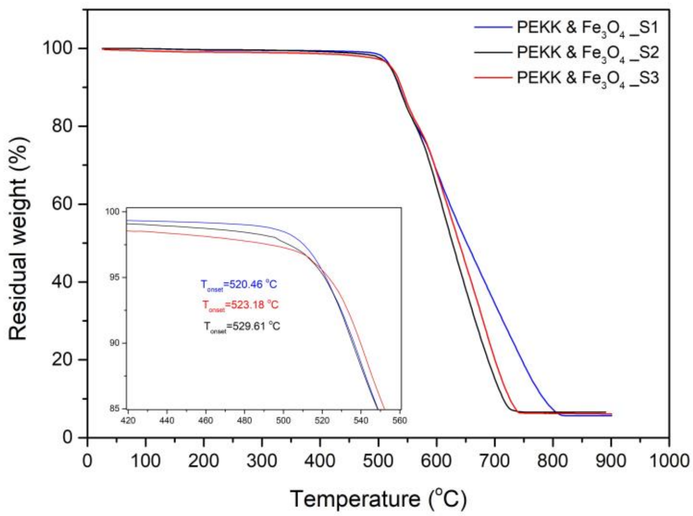

Figure *9***.** Comparative TGA thermograms for each processing stage, namely pellet form (S1), FFF interlayer (S2), after re-melting with induction heating (S3).

Figure 10 represents the DSC thermograms for each processing stage. The plots present the second heating and cooling cycles, employed for the calculation of thermodynamic quantities. From this analysis, the nanocomposites have a glass transition temperature (T_g) of 159°C, same as the value reported for the pure pseudo amorphous PEKK matrix [40]. The addition of magnetic nanoparticles has a moderate nucleation effect in the polymer matrix, with cold crystallization peaks appearing at 261-263 °C for all processing stages, followed by melting peaks at 306-307 °C. The melting region for all samples tested was found below 320°C, which was set as the minimum temperature required to achieve debonding during induction heating.

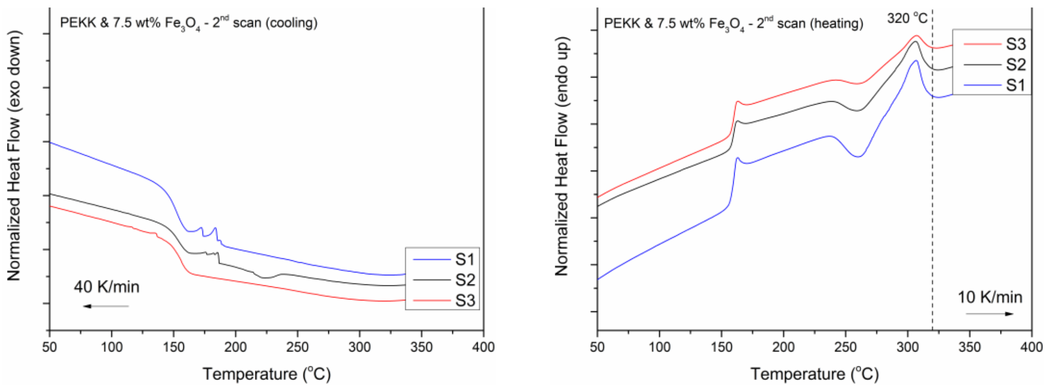

Figure 10. DSC thermograms for each processing stage, namely pellet form (S1), FFF interlayer (S2), after re-melting with induction heating (S3). Right: 2nd scan heating cycles; Left: cooling cycle.

Table 4. DSC estimated values of thermodynamic quantities and TGA thermal degradation onset temperature for PEKK & 7.5wt.% samples at different processing stages. Crystallization temperature (T_c) and enthalpy (ΔH_c), glass transition temperature (T_g), cold crystallization temperature (T_{cc}) and enthalpy (ΔH_{cc}), melting peak temperature (T_m) and enthalpy (ΔH_m), onset decomposition temperature ($T_{o/95\%}$) corresponding to 5% weight loss of the initial mass.

Sample	DSC scan 2							TGA
	Cooling		Heating					
	T_c (°C)	ΔH_c (J/g)	T_g (°C)	T_{cc} (°C)	ΔH_{cc} (J/g)	T_m (°C)	ΔH_m (J/g)	$T_{o/95\%}$ (°C)
S1	-	0	159	262	5	307	6	520.5
S2	221	1	159	261	4	306	7	529.6
S3	-	0	159	263	3	307	4	523.2

3.3 Coupon-level mCT inspection

Assessment of the internal structure of composite laminate specimens was conducted via mCT scanning. A reference sample was scanned before treatment at a 5.5 μm voxel size. Top/bottom CFRP laminates have a high compaction degree with minimum defects. In the case of the FFF nanocomposite layer, a high degree of porosity was observed for Type I specimens, with variable pore and NP agglomerate sizes (Figure 11). In comparison with mCT analysis conducted in Section 3.1, where no porosity was observed in specimens of the same NP concentration obtained from FFF filament samples (Figure 6), it may be derived that this effect is introduced during the FFF process. Nonetheless, as far as the debonding functionality of the nanocomposite material is concerned, there was no significant variation during induction heating for the parameters tested, thus indicating that the effect of porosity, if any, was the same for all specimens investigated. An improved compaction and uniformity of the FFF nanocomposite layer was obtained for Type II specimens, as it can be observed in Figure 12.

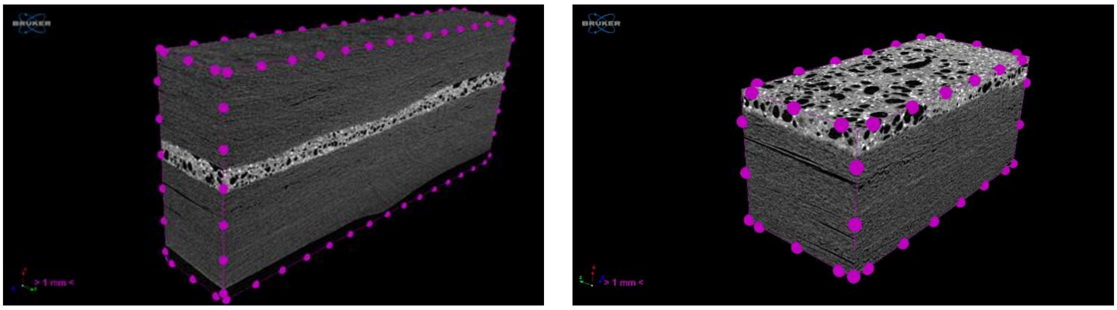

Figure 11. 3D visualization of Type I specimen and FFF nanocomposite interlayer before induction heating (white regions: FFF interlayer and NP agglomerates, grey region: CFRP/polymer matrix, black: background/ air; scale bar: 1 mm).

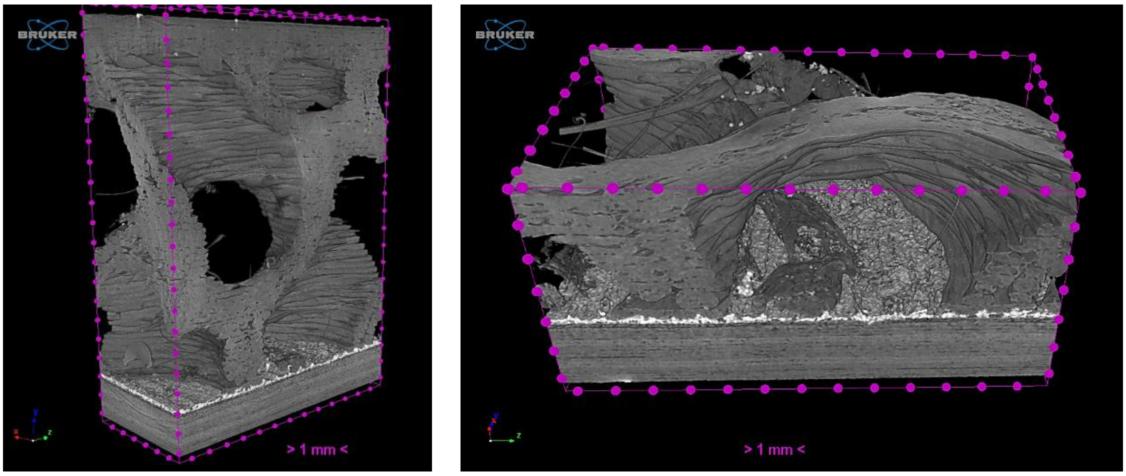

Figure 12. 3D visualization of Type II specimen and FFF nanocomposite interlayer before induction heating (white regions: FFF interlayer and NP agglomerates, grey region: CFRP/polymer matrix, black: background/ air; scale bar: 1 mm).

3.4 Induction Heating Capacity Assessment

3.4.1 Induction Simulation

The absolute value of the induced magnetic field intensity H was simulated for the FFF debonding zone, considering different standoff distances away from the coil and different generator power/frequency settings, as shown in Figure 13a & b. Based on the defined induction process parameters (Table 3) and simulation results, magnetic field intensities in the range of 1-5 kA m^{-1} were experimentally tested. The effect of generator power on magnetic field intensity becomes more pronounced with decreasing standoff distance (Figure 13a), with up to 25% higher intensity simulated for 3kW power in comparison with 2kW for 20 mm standoff distance. When comparing the high/low levels of standoff distance for different frequencies (calculated automatically by the RF generator by the defined power setpoints, Table 3), it is confirmed that workpiece to coil distance has a prominent contribution to magnetic field intensity (Figure 13b). With the increasing coil distance from the FFF debonding zone, the magnetic field strength and gradient decrease, thus better temperature uniformity can be achieved (Figure 14). Based on simulation results and preliminary experimental trials, induction heating process development was conducted within 2-3kW generator power range, for 20-45 mm standoff distances, aiming to identify the optimum trade-off between process parameters that promote temperature increase above PEKK melting region and facilitate debonding, without specimen overheating. Stand-off distances below 20 mm, corresponding to magnetic field intensities in the range of 8-10 kA m^{-1}, resulted in a steep temperature increase and specimen overheating, thus were not included in the analysis.

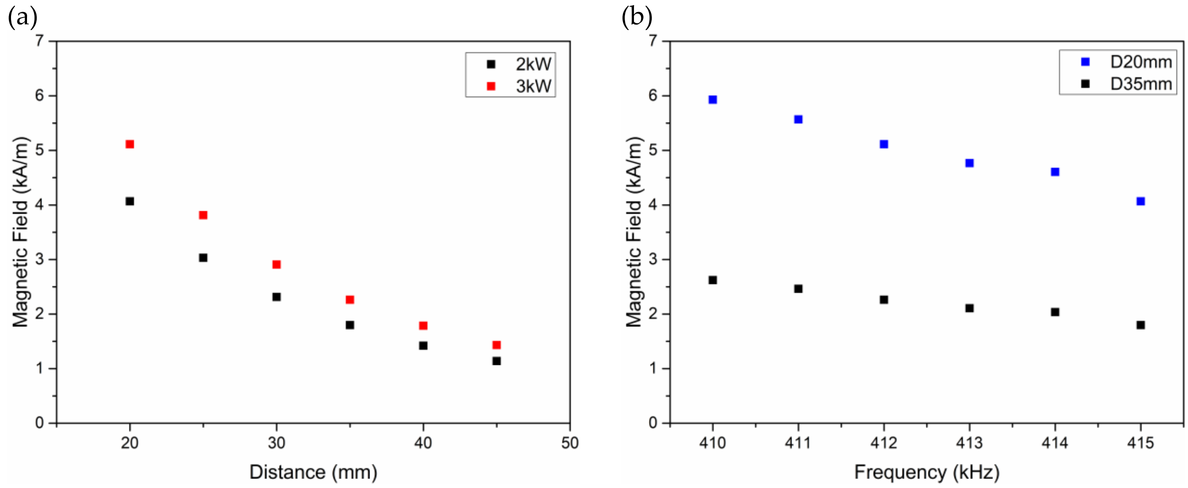

Figure 13. Absolute value of the induced magnetic field intensity H simulated for different standoff distances and generator power/frequency settings. 528 529

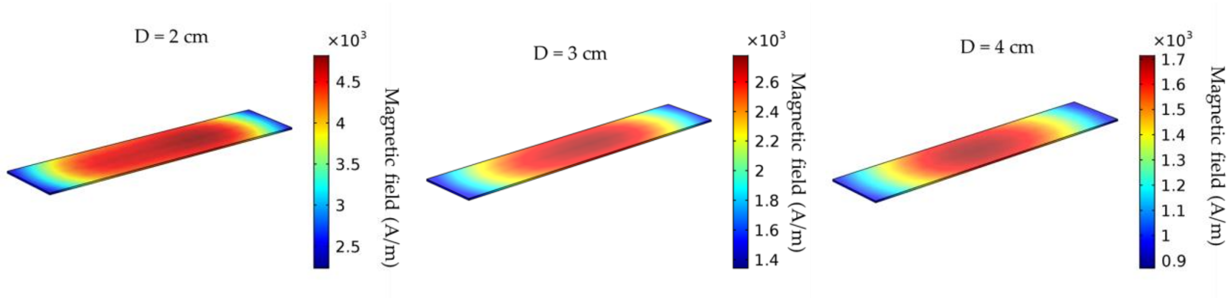

Figure 14. Magnetic field intensity H simulated for the FFF debonding zone located at different standoff distances from the coil. 530 531

3.4.2 Induction heating assessment 532

3.4.2.1 Reference laminate testing 533

As a preparatory step prior to testing, reference PAEK laminates were investigated to confirm that they are electromagnetically inert within the range of experimental conditions tested, and that no heating is induced by the application of the RF field. As shown in Figure 15, no increase in specimen temperature was recorded, thus ensuring that induction heating only derives from the nanocomposite FFF interlayer. 534 535 536 537 538

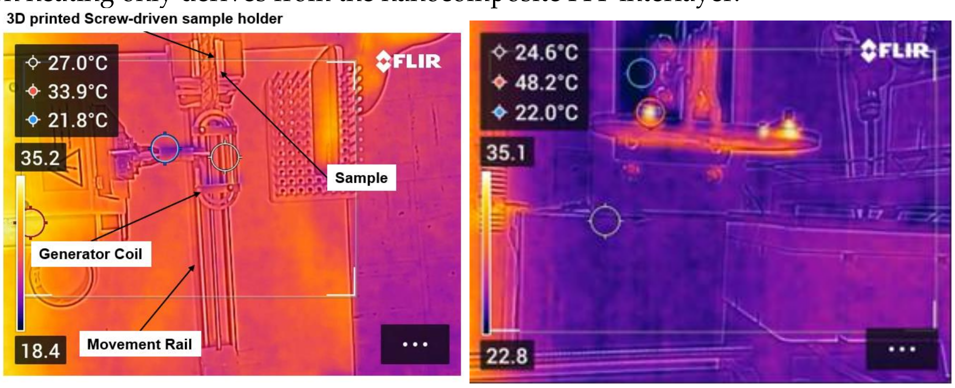

539

Figure 15. Left: Top-view image of the automated movement setup captured with the IR camera; Right: Measurement of reference PAEK sample without nanocomposite FFF interlayer – no increase in specimen temperature recorded. 540 541 542

543

3.4.2.2 Type I Specimens

Induction heating experiments of Type I specimens were performed at varying standoff distances (distance between the debonding zone and the coil) and power values, to define the optimum process parameters that can facilitate debonding. In particular, standoff distance values ranged from 20 mm to 45 mm, while applied power values ranged from 2 kW to 3 kW. Initially, experiments were performed with regards to varying standoff distance values, while the applied power was maintained stable at 2 kW and 3 kW respectively.

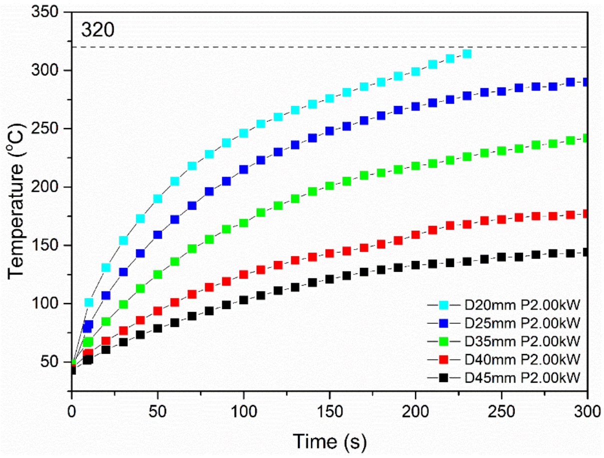

Figure 16. Representative induction heating curves of Type I specimens at 2 kW power value and varying standoff distance values (20-45 mm).

The induction heating results for the Type I specimens tested at 2 kW power and varying standoff distance values, are presented in Figure 16. Therein, the impact of standoff distance can be identified. In detail, the increase of standoff distance limits the induction heating performance of specimens. Also, specimens tested at standoff distance values from 25 mm to 45 mm, were heated at a steady rate, followed by various temperature plateaus at values lower than 300 °C. Considering that the specimen debonding is facilitated by the melting state of PEKK (T_m=320 °C), the respective set of parameters cannot be applied for the debonding process. However, specimen testing at a standoff distance of 20 mm exhibited temperature increase at 320 °C after 220 s of measurement time, demonstrating enhanced induction heating capacity. This finding indicates that a standoff distance value of 20 mm, while applying 2 kW of power, can induce sufficient temperature increase in the debonding zone, so that the specimen can be debonded, using the continuous un-zipping mechanism.

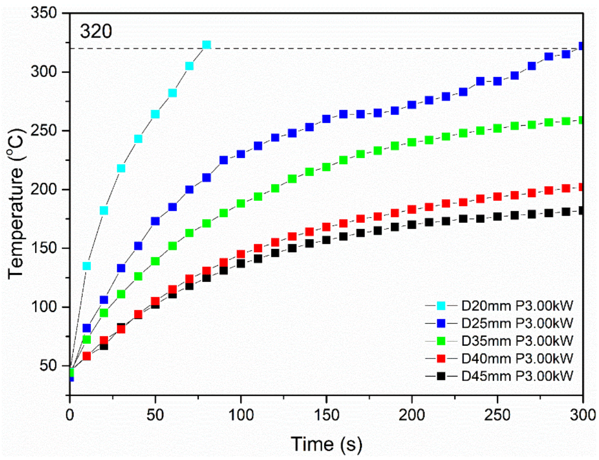

Figure 17. Representative induction heating curves of Type I specimens at 3 kW power value and varying standoff distance values (20-45 mm).

Experiments were repeated, with the same standoff distance values, while employing 3 kW of power. The respective induction heating results (Figure 17), indicate the same trend regarding the impact of standoff distance in the heating performance of specimens. Despite the fact that the increase in power resulted in enhanced heating performance for all specimens, temperature plateaus were identified at values lower than 250 °C, for specimens tested at standoff distance values ranging from 35 mm to 45 mm. Specimens tested at standoff distance of 20 mm and 25 mm were heated above the melting temperature of pure PEKK (T_m=320 °C), indicating that these sets of parameters can be applied in order to study the specimen debonding.

Collectively, results obtained from the induction heating experiments at power values of 2 kW and 3 kW, indicated that the specimens were effectively heated above the melting temperature of pure PEKK when the standoff distance was either 20 mm (for both 2 kW and 3 kW) or 25 mm (for 3 kW). For standoff distances over 35 mm, a temperature plateau is reached due to thermal losses by conduction into the specimen or by convection into the surrounding ambient air. As standoff distance of 20 mm was critical in facilitating debonding in both cases of applied power, the process optimization was finalized with induction heating experiments conducted at 20 mm standoff distance and varying power values ranging from 2 kW to 3 kW, with an increment of 0.25 kW per trial (Figure ***18***).

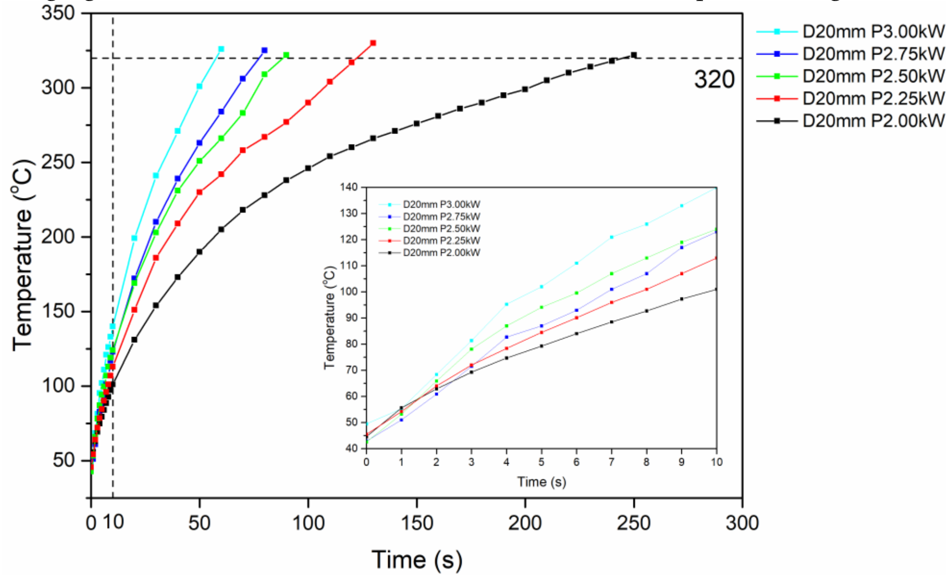

Figure *18***.** Representative induction heating curves of Type I specimens at 20 mm standoff distance and varying power values (2 kW - 3 kW).

Based on the results of the induction heating experiments conducted at constant standoff distance and varying power values (Figure 18), it can be observed that all specimens were heated at temperatures higher than the melting temperature of pure PEKK, indicating that all sets of parameters can be applied for the investigation of specimen debonding. By adjusting generator power, initial heating rates within the range of 5.3 – 9.4 ^{0}C/s were achieved, with all specimens tested reaching the targeted temperature for debonding, i.e. above 320 °C. Specimens tested with power values from 2.5 kW to 3 kW were heated above 320 °C, within less than 90 s of RF field exposure, while specimens tested at 2 kW and 2.25 kW, exceeded the specific temperature after 130 s and 250 s of measurement time respectively (Table 5). Overall power values of 2.5, 2.75, and 3 kW presented similar performance for fast sample heating, while 2 and 2.25 kW values provide a slower heating rate that can facilitate heat dissipation and promote temperature uniformity.

Table 5. Initial heating rate over 0-10 s and time to reach debonding temperature for 20 mm standoff distance within 2-3kW power range tested with Type I specimens.

Type I / D = 20 mm	P = 2.00 kW	P = 2.25 kW	P = 2.50 kW	P = 2.75 kW	P = 3.00 kW
Initial heating rate [t = 0-10 s] (⁰C/s)	5.3 ± 0.3	6.5 ± 0.2	8.0 ± 0.4	7.9 ± 0.3	9.4 ± 0.4
Time to reach debonding T>320ᵒC (s)	250	130	90	80	60

3.4.2.3 Type II Specimens

Based on results obtained from induction heating assessment of Type I specimens, the process window of 2-3 kW power at 20 mm standoff distance presented a promising heating performance, with all sets of process parameters (standoff distance, power) being able to induce sufficient temperature increase above PEKK melting temperature range in the specimen debonding zone. Subsequently, the defined process window was further tested with Type II (Gyroid) specimens, to assess the effect of FFF interlayer integration in a more complex geometry.

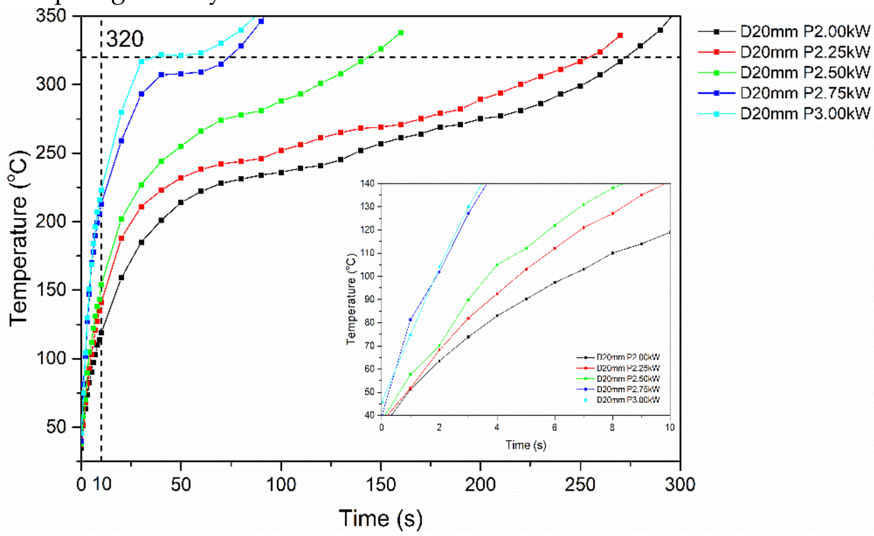

Figure *19***.** Representative induction heating curves of Type II (Gyroid) specimens at 20 mm standoff distance and varying power values (2kW-3kW).

Based on the trial results presented in Figure ***19***, all specimens were heated above the melting temperature of PEKK (320 ᵒC), with initial heating rates within the range of 8.0 – 17.5 ⁰C/s, thus all experimental conditions tested were within the debonding window definition for Type II specimens. Results for Type II specimens follow the same trend as in Type I, with 2 and 2.25 kW power values providing a slower heating rate and reaching debonding temperature after 250 s (Table 6). Further, specimens tested at 2.75 kW and 3 kW of power exhibited higher heating rates, reaching debonding temperature under 70 s of RF field exposure, indicating a larger influence of the power applied to the testing. For equivalent FFF interlayer active surface area, higher initial heating rates were demonstrated in Type II specimens, possibly associated differences in magnetic flux density due to specimen geometry as well as the higher degree of compaction and lack of porosity observed in Type II specimens. In addition, it should be noted that Type II specimens demonstrated temperature plateaus which, in contrast to the plateaus observed in Type I specimens as result of thermal losses, were followed by a steady temperature increase which eventually exceeded the targeted debonding temperature. The presence of these plateaus can be attributed to the geometry and material characteristics of Type II gyroid specimens, as the gyroid structure consisting of pure PEKK is adjacent to the nanocomposite debonding area, which facilitates heat dissipation and possibly induces local endothermic phase changes in its proximity [41]. This effect becomes more pronounced in 3.00 and 2.75 kW power values, in temperatures near PEKK matrix melting region, where temperature plateaus appear at approximately 25 s and 40 s of measurement time respectively. Results indicate that a high heating rate can be combined with a steady-temperature time interval in which debonding can be conducted without compromising laminate quality. Although this effect could not be fully assessed due to lack of thermal insulation in the sample, it will further be studied and exploited in future experiments as a promising time frame for debonding.

Table 6. Initial heating rate over 0-10 s and time to reach debonding temperature for 20 mm standoff distance within 2-3kW power range tested with Type II specimens.

Type II / D = 20 mm	P = 2.00 kW	P = 2.25 kW	P = 2.50 kW	P = 2.75 kW	P = 3.00 kW
Initial heating rate [t = 0-10 s] (^{0}C/s)	8.0 ± 0.5	10.2 ± 0.5	11.1 ± 0.7	16.5 ± 1.5	17.5 ± 1.3
Time to reach debonding T>320^{o}C (s)	270	250	140	70	40

3.4.2.4 Debonding of Type I and II specimens & inspection

Following the static induction heating trials in Type I and Type II specimens, the process window of 2-3 kW power at 20 mm standoff distance was further employed for debonding trials. Specifically, each specimen was placed in the mounting setup as described in Section 2.4.1, and the debonding zone was carefully aligned with the ceramic blade position, by adjusting the height of the latter. The mounting setup was set in linear motion when the recorded temperature reached 320^{0}C, and specimens were moved towards the ceramic blade at a constant linear speed of 2.0 mm/s (Figure 20 & Figure 21). In all specimens tested (Type I and II) full unzipping of the FFF debonding zone was achieved. Subsequently, CFRP laminate samples retrieved from debonded specimens were further analyzed to assess their quality and morphology of the nanocomposite layer.

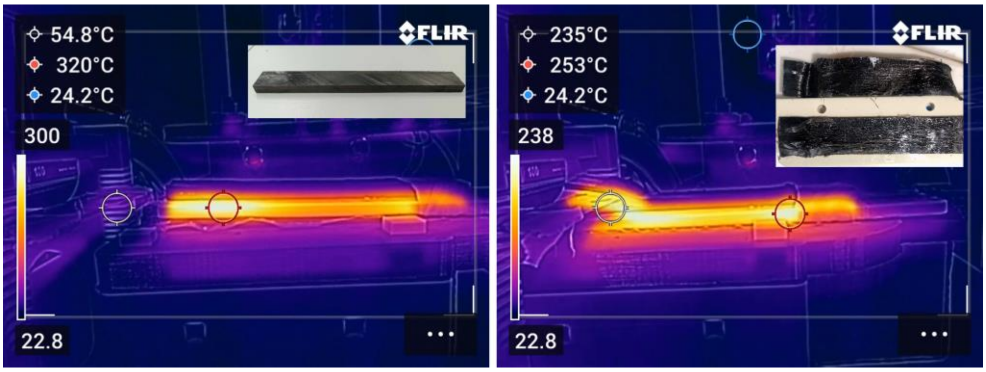

Figure 20. Indicative thermal camera images of debonding of Type I specimens, coupled with specimen structure prior and after debonding.

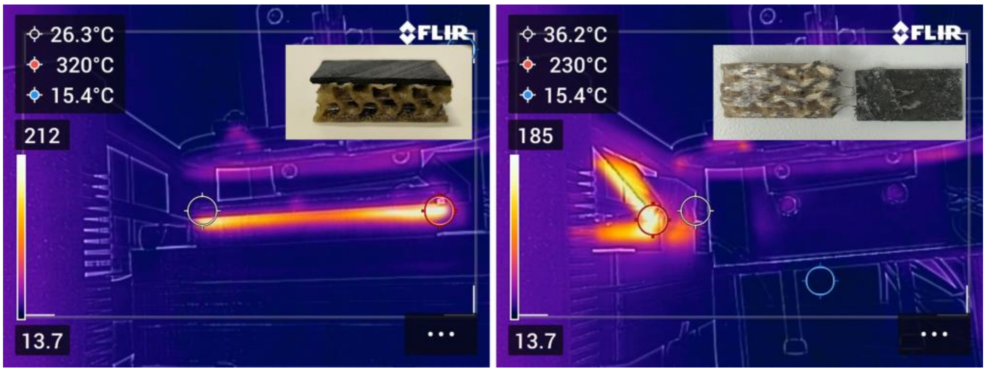

Figure 21. Indicative thermal camera images of debonding of Type II specimens, coupled with specimen structure prior and after debonding.

Initially, cross-sections of debonded CFRP laminates were inspected via optical microscopy to assess any visible indications of overheating and delamination. As observed in Figure 22, there is no evident impact on laminate quality when the applied power ranges from 2 kW to 2.5 kW, while delamination starts to occur for 2.75 kW and overheating becomes more pronounced for 3kW generator power. Additionally, the debonded surface morphology for the two marginal power values (2kW and 3kW) is depicted in Figure 23, where the effect of induction heating process conditions is observed in the resulting FFF debonding zone residues and surface texture transition from rough to smooth, fully melted state. In Figure 24, the respective debonded constituents of Type II gyroid specimen processed under 2kW generator power at 20 mm standoff distance can be observed, where residues of the FFF debonding zone can be seen around the previous contact points among the gyroid structure and CFRP laminate (Figure 24c).

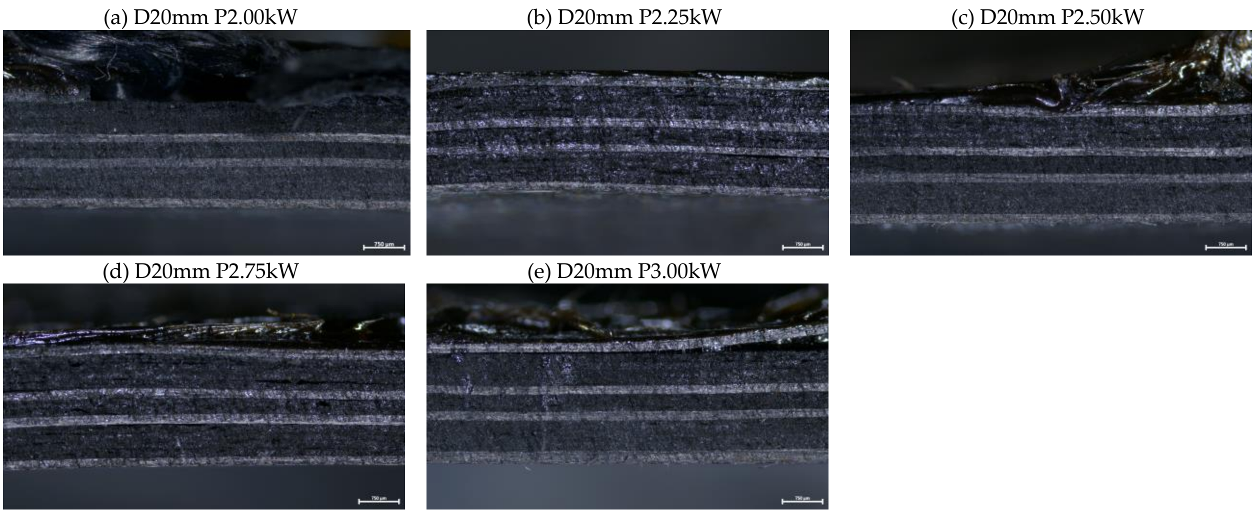

Figure 22. Cross-section images of debonded CFRP laminates extracted from Type I specimens processed under 2-3kW generator power range at 20 mm standoff distance (scale bar: 750 um).

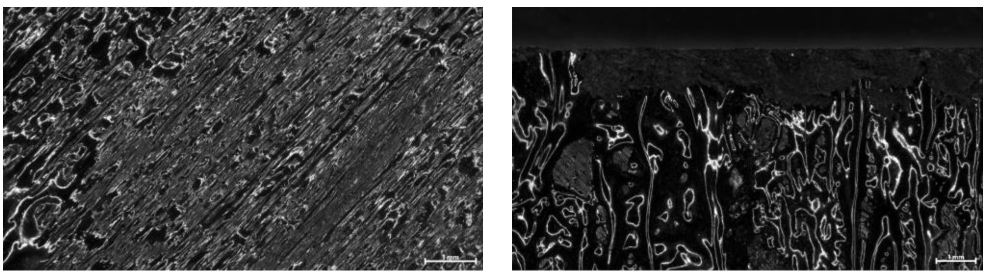

Figure 23. Top-view images of debonded surface morphology for 2 kW (left) and 3 kW (right) generator power at 20 mm standoff distance (scale bar: 1 mm)

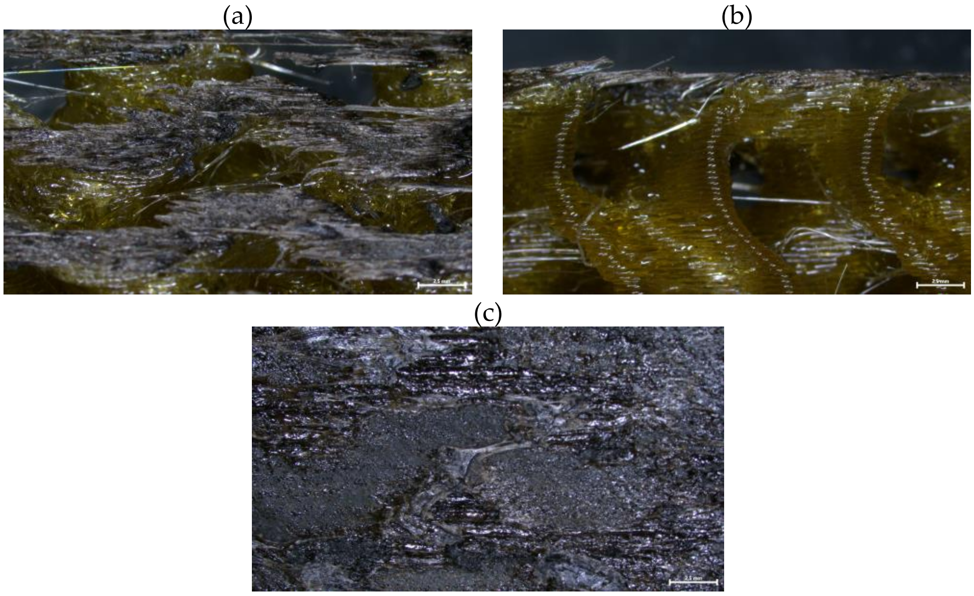

Figure 24. Top (a) and side (b) view of debonded gyroid structure and CFRP laminate (c) of Type II specimen processed under 2kW generator power at 20 mm standoff distance (scale bar: 2.5 mm)

SEM coupled with EDS analysis was conducted to further study the morphology of the nanocomposite layer and perform elemental analysis. EDS was employed to identify possible traces of the Fe_3O_4 agglomerates in the PEKK matrix of the debonding zone; Fe_3O_4 agglomerates were observed in all debonded surfaces with sizes ranging from 10 μm to 30 μm. This finding is also depicted in the EDS analysis (Figure 25f) through the distinct O and Fe peaks. It should be noted that peaks corresponding to approximately 2 keV represent the presence of Au traces, which is attributed to the sputter-coating of all specimens prior to SEM characterization. All debonded specimens exhibited surface transformations in the intermediate layer, which correspond to the melting of the nanocomposite layer. During the disassembly process, the nanocomposite layer may be completely or partially detached from the adjacent LMPAEK-CFs layers, due to the separation mechanism employed. A moderate contribution of the tape layup direction employed in AFP manufacturing can be observed in surface morphology, with directionality of tape-laying morphology propagating from the CFRP laminate to the subsequent FFF interlayer (Figure 25a-d).

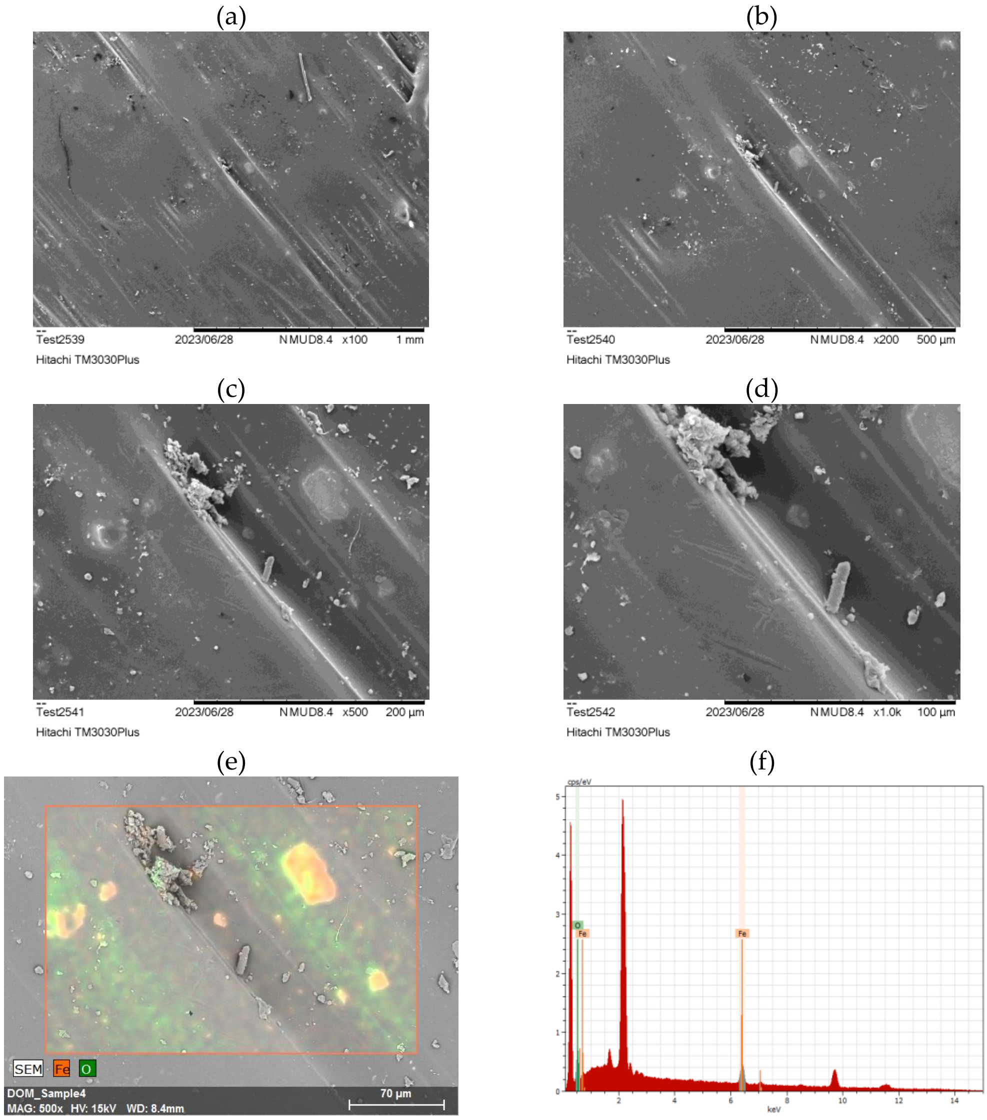

Figure 25. SEM morphology images (a-d) and EDS elemental analysis (e-f) of the intermediate layer (debonding zone) of debonded specimen.

Finally, assessment of the internal structure of debonded CFRP laminates was conducted via mCT scanning. A reference sample was scanned at 5.5 um voxel size after induction heating treatment and debonding. The debonded surface morphology presents a wavy texture due to remelting and detachment, while a clean detachment without residue is observed at the corner of the specimen, indicating that complete removal of the FFF interlayer is feasible upon further optimization of the ceramic blade positioning. A small degree of delamination in PAEK CFRP is observed due to the heat treatment, however the overall structural integrity is maintained.

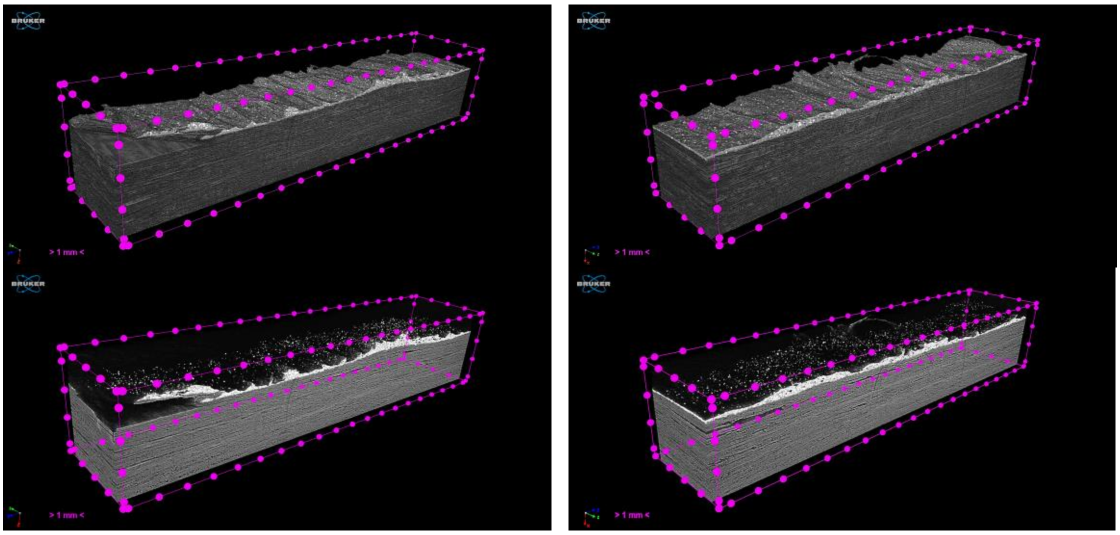

Figure 26. 3D visualization of CFRP laminate and residual FFF nanocomposite interlayer after induction heating and debonding (white regions: NP agglomerates, grey region: CFRP/polymer matrix, black: background/ air). Top/bottom images were obtained by adjustment of the attenuation coefficient range to isolate features with different absorptivity (scale bar: 1mm).

4. Conclusions

In this study, localized induction heating and debonding of sandwich-structured composite laminate panels was investigated in testing coupons prepared by AFP and extrusion-based AM technologies. By exploiting advanced composite manufacturing technologies, the integration of discrete debonding zones in two types of sandwich-structured laminate composites has been demonstrated. Induction heating and thus, debonding was primarily enabled by the incorporation of nanocomposite interlayers (debonding zones) consisting of Poly-ether-ketone-ketone (PEKK) and ferrimagnetic iron oxide (Fe_3O_4) nanoparticles acting as electromagnetic susceptors. To investigate induction heating performance and debonding feasibility, a bespoke experimental setup was developed, allowing to optimize the induction heating process parameters and effectively separate different layers of laminate composites.

Based on magnetic field simulation results and preliminary experimental trials, induction heating process development was conducted within 2-3 kW generator power range, for 20-45 mm standoff distances from the coil, corresponding to low magnetic field intensities in the range of 1-5 kA m^{-1}. Simultaneous thermal imaging enabled the identification of critical process parameters aiming to achieve an optimum trade-off between temperature increase above melting point of pure PEKK (T_m = 320 ^{o}C), which would enable the effective melting of the debonding zone without specimen overheating. Results obtained indicated that the specimens were effectively heated above the melting temperature of pure PEKK when the standoff distance was 20 mm (for both 2 kW and 3 kW) or 25 mm (for 3 kW). By adjusting generator power for a standoff distance of 20 mm, initial heating rates within the range of 5.3 – 9.4 ^{0}C/s were achieved for Type I and 8.0 – 17.5 ^{0}C/s for Type II specimens respectively. In both specimen types, 2 kW power value provided a slower heating rate, reaching debonding temperature after 250 s. All specimens were heated at temperatures higher than the melting temperature of pure PEKK, thus allowing the definition of the debonding process window that was further tested after static heating experiments.

For debonding trials, each specimen was placed in the mounting setup and the debonding zone was carefully aligned with a ceramic blade. The mounting setup was set in linear motion when the recorded temperature reached 320^{0}C, and specimens were moved at a constant linear speed of 2.0 mm/s. In all specimens tested (Type I and II) full unzipping of the FFF debonding zone was achieved. Subsequently, CFRP laminate samples retrieved from debonded specimens were further analyzed to assess their quality and the morphology of the nanocomposite layer. The outcomes of this study provide an initial baseline for the development of rapid, on-demand joining, repair and disassembly technologies for thermoplastic composites, towards new Design for Disassembly strategies and more efficient Maintenance, Repair and Overhaul operations. Future research directions aim at the optimization of nanoparticle dispersion and further analysis of dynamic rheological and thermal properties of the nanocomposite, as well as the assessment of joint mechanical performance, to establish reliable process-structure-property-performance relationships for the design and integration of debonding zones in more complex joint geometries, as well as investigation of repair, remanufacturing and repurposing strategies of laminate composites to improve their circularity and performance.

Author Contributions: Conceptualization, E.G., K.Z., C.T. and T.K.M.; methodology, E.G., K.Z., C.T., A.P., A.R., P.R.R., T.K.M., and G.P.G.; validation, E.G., K.Z., and C.T.; formal analysis, E.G., K.Z., T.K.M., and G.P.G.; investigation, E.G., K.Z., C.T., A.P., A.R., P.R.R., T.K.M., and G.P.G.; data curation, E.G., K.Z., C.T., A.P., A.R., P.R.R., A.K. and G.P.G.; writing—original draft preparation, E.G., K.Z., G.P.G., A.P., A.R., P.R.R., A.K. and C.T.; writing—review and editing, E.G., K.Z., P.R.R, and T.M.K.; supervision, C.A.C.; funding acquisition, C.A.C. All authors have read and agreed to the published version of the manuscript.

Funding: This work was funded by the European Union's Horizon 2020 Research and Innovation Action entitled: 'Digital method for imprOved Manufacturing of next-generation MultIfuNctIOnal airframe parts' (DOMMINIO) under GA No. 101007022.

Data Availability Statement: The original contributions presented in the study are included in the article/supplementary material, further inquiries can be directed to the corresponding author/s.

Acknowledgments: The authors would like to thank Dr. Panagiotis Maroulas for his assistance on thermogravimetric measurements.

Conflicts of Interest: The authors declare no conflicts of interest. The funders had no role in the design of the study; in the collection, analyses, or interpretation of data; in the writing of the manuscript; or in the decision to publish the results.

Appendix A

For the development of the computational model, the following governing equations were used:

$$\nabla \times \boldsymbol{H} = \boldsymbol{J} \tag{1}$$

$$\boldsymbol{B} = \nabla \times \boldsymbol{A} \tag{2}$$

$$\boldsymbol{E} = \mathrm{j}\omega \boldsymbol{A} \tag{3}$$

$$\boldsymbol{J} = \sigma E + j\omega \boldsymbol{D} \tag{4}$$

where H is the magnetic field intensity, E is the electric field strength, B is the magnetic flux density, J is the current density vector, σ is the electrical conductivity and A is the magnetic vector potential. The set of equations is completed by the following relations:

$$\mathbf{B} = \mu_0 \mu_r \boldsymbol{H} \tag{5}$$

$$\boldsymbol{D} = \varepsilon_0 \varepsilon_r \boldsymbol{E} \tag{6}$$

where μ_r is the relative permeability and ε_r is the relative permittivity. A bounding box around the experimental setup is selected to model the surrounding air around the geometry, and a magnetic insulation boundary condition is imposed on the bounding box boundaries:

$$\boldsymbol{n} \times \boldsymbol{A} = 0 \tag{7}$$

The size of the bounding box size was determined by increasing the box size until the model results are unaffected by further size increase. The coil was simulated by imposing the respective experimental conditions of Table 3. The conductivity and permittivity of the different materials was taken from the experimental measurements and the equipment manufacturer data sheet. A computational mesh of 197247 elements was used to discretize the computational domain, and a quadratic basis function was used for the dependent variables. The set of equations was solved using COMSOL Multiphysics.

References

1. Ozturk F, Cobanoglu M, Ece RE. Recent advancements in thermoplastic composite materials in aerospace industry. Journal of Thermoplastic Composite Materials. 2024;37(9):3084-3116 https://doi.org/10.1177/08927057231222820
2. Heathman N., Koirala P., Yap T., Emami A., Tehrani M. In situ consolidation of carbon fiber PAEK via laser-assisted automated fiber placement, Composites Part B: Engineering, 2023 (249): 110405 https://doi.org/10.1016/j.compositesb.2022.110405
3. Yousefpour A, Hojjati M, Immarigeon J-P. Fusion Bonding/Welding of Thermoplastic Composites. Journal of Thermoplastic Composite Materials. 2004;17(4):303-341 https://doi.org/10.1177/0892705704045187
4. Lambiase F., Grossi V., Paoletti A., High-speed joining of hybrid metal-polymer joints during the friction-assisted joining process, Composite Structures 2022 (280): 114890 https://doi.org/10.1016/j.compstruct.2021.114890
5. Reis, J.P.; de Moura, M.; Samborski, S. Thermoplastic Composites and Their Promising Applications in Joining and Repair Composites Structures: A Review. Materials 2020, 13, 5832. https://doi.org/10.3390/ma13245832
6. Gouin O'Shaughnessey P, Dubé M, Fernandez Villegas I. Modeling and experimental investigation of induction welding of thermoplastic composites and comparison with other welding processes. Journal of Composite Materials. 2016;50(21):2895-2910 https://doi.org/10.1177/0021998315614991
7. Banea, M.D. Debonding on Demand of Adhesively Bonded Joints. In Progress in Adhesion and Adhesives, K.L. Mittal (Ed.) (2020) https://doi.org/10.1002/9781119749882.ch2
8. Farahani, R.D. and Dubé, M., Novel Heating Elements for Induction Welding of Carbon Fiber/Polyphenylene Sulfide Thermoplastic Composites. Adv. Eng. Mater., 2017 19: 1700294. https://doi.org/10.1002/adem.201700294
9. Li M, Wen L, Wang S, Liang J, Hou X. Multifactor optimization for induction welding of carbon fiber reinforced thermoplastic composites based on response surface methodology. Polym Compos. 2024; 45(5): 4307-4318. https://doi.org/10.1002/pc.28060
10. Tavakoli MH, Karbaschi H, Samavat F. Influence of workpiece height on the induction heating process, Mathematical and Computer Modelling, 2011 (54):50-58 https://doi.org/10.1016/j.mcm.2011.01.033
11. Mariani, A.; Malucelli, G. Insights into Induction Heating Processes for Polymeric Materials: An Overview of the Mechanisms and Current Applications. Energies 2023, 16, 4535. https://doi.org/10.3390/en16114535
12. Yu, X., Yang, R., Wu, C. et al. The heating efficiency of magnetic nanoparticles under an alternating magnetic field. Sci Rep 12, 16055 (2022). https://doi.org/10.1038/s41598-022-20558-0
13. Dutz, S., & Hergt, R. Magnetic nanoparticle heating and heat transfer on a microscale: Basic principles, realities and physical limitations of hyperthermia for tumour therapy. International Journal of Hyperthermia, 2013 29(8), 790–800. https://doi.org/10.3109/02656736.2013.822993
14. Raczka T., Wolf A., Reichstein J., Stauch C., Schug B., Müssig S., Mandel K., Influence of magnetic interactions in iron oxide nanoparticle polymer composites on magnetism and induction heating, Journal of Magnetism and Magnetic Materials, 2024 (598):172042, https://doi.org/10.1016/j.jmmm.2024.172042
15. Eggeman A. S., Majetich S. A., Farrell D., Pankhurst Q. A., Size and Concentration Effects on High Frequency Hysteresis of Iron Oxide Nanoparticles, IEEE Transactions on Magnetics, 2007 (43):2451-2453, https://doi.org/10.1109/TMAG.2007.894127
16. Martin R.G., Johansson C., Tavares J.R., Dubé M., Manufacturing of thermoplastic composite sandwich panels using induction welding under vacuum, Composites Part A: Applied Science and Manufacturing, 2024 (182): 108211 https://doi.org/10.1016/j.compositesa.2024.108211
17. Garaio E., Collantes J.M., Garcia J.A., Plazaola F., Mornet S., Couillaud F., Sandre O., A wide-frequency range AC magnetometer to measure the specific absorption rate in nanoparticles for magnetic hyperthermia, Journal of Magnetism and Magnetic Materials, 2014 (368): 432-437, https://doi.org/10.1016/j.jmmm.2013.11.021
18. Díez A.G., Rincón-Iglesias M., Lanceros-Méndez S., Reguera J., Lizundia E., Multicomponent magnetic nanoparticle engineering: the role of structure-property relationship in advanced applications, Materials Today Chemistry, 2022 (26): 101220 https://doi.org/10.1016/j.mtchem.2022.101220
19. Bayerl T., Duhovic M., Mitschang P., Bhattacharyya D., The heating of polymer composites by electromagnetic induction – A review, Composites Part A: Applied Science and Manufacturing, 2014 (57): 27-40 https://doi.org/10.1016/j.compositesa.2013.10.024.
20. Obaidat, I.M.; Issa, B.; Haik, Y. Magnetic Properties of Magnetic Nanoparticles for Efficient Hyperthermia. Nanomaterials 2015, 5, 63-89. https://doi.org/10.3390/nano5010063
21. Mohapatra, J.; Xing, M.; Liu, J.P. Inductive Thermal Effect of Ferrite Magnetic Nanoparticles. Materials 2019, 12, 3208. https://doi.org/10.3390/ma12193208
22. Almind M. R., Vinum M. G., Wismann S. T., Hansen M. F., Vendelbo S. B., Engbæk J. S., Mortensen P. M., Chorkendorff Ib, and Frandsen C., ACS Applied Nano Materials 2021 4 (11), 11537-11544 https://doi.org/10.1021/acsanm.1c01941

23. Fantechi E., Innocenti C., Albino M., Lottini E., Sangregorio C., Influence of cobalt doping on the hyperthermic efficiency of magnetite nanoparticles, Journal of Magnetism and Magnetic Materials, 2015 (380):365-371, https://doi.org/10.1016/j.jmmm.2014.10.082
24. Bae, D.H., Shon, M.Y., Oh, S.T. and Kim, G.N. Study on the Heating Behavior of Fe3O4-Embedded Thermoplastic Polyurethane Adhesive Film via Induction heating. Bull. Korean Chem. Soc., 2016, 37: 1211-1218. https://doi.org/10.1002/bkcs.10841
25. Bae D., Shin P., Kwak S., Moon M., Shon M., Oh S., Kim G., Heating behavior of ferromagnetic Fe particle-embedded thermoplastic polyurethane adhesive film by induction heating, 2015, Journal of Industrial and Engineering Chemistry (30):92-97, https://doi.org/10.1016/j.jiec.2015.05.007
26. Baek, I.; Lee, S. A Study of Films Incorporating Magnetite Nanoparticles as Susceptors for Induction Welding of Carbon Fiber Reinforced Thermoplastic. Materials 2020, 13, 318. https://doi.org/10.3390/ma13020318
27. Cheng X., Zhou Y., Charles A.D.M., Yu Y., Islam M.S., Peng S., Wang J., Rider A.N., Lim M., Timchenko V., Wang C., Enabling contactless rapid on-demand debonding and rebonding using hysteresis heating of ferrimagnetic nanoparticles, Materials & Design, 2021 (210):10076, https://doi.org/10.1016/j.matdes.2021.110076
28. Alvarez E.M., Quintana González S.A., Lopez Taborda L.L. and Niebles Nuñez E.E. Experimental study of adhesive joints with mechanical interlocking of acrylonitrile butadiene styrene (ABS) parts fabricated for fused filament (FFF), Rapid Prototyping Journal, 2023 (29):1984-2000. https://doi.org/10.1108/RPJ-04-2023-0146
29. Frascio M., Moroni F., Marques E., Carbas R., Reis M., Monti M., Avalle M., da Silva L.F.M., Feasibility study on hybrid weld-bonded joints using additive manufacturing and conductive thermoplastic filament, Journal of Advanced Joining Processes, 2021 (3):100046, https://doi.org/10.1016/j.jajp.2021.100046.
30. Marques, J. B., Barbosa, A. Q., da Silva, C. I., Carbas, R. J. C., & da Silva, L. F. M. An overview of manufacturing functionally graded adhesives – Challenges and prospects. The Journal of Adhesion, 2019, 97(2), 172–206. https://doi.org/10.1080/00218464.2019.1646647
31. Ecker J., Liska R., Stampfl J., Design for disassembly: Using a multi-material approach in 3D printing for easier recycling strategies, Additive Manufacturing, 2024 (92):104394, https://doi.org/10.1016/j.addma.2024.104394.
32. Galarreta-Rodriguez, I., Lopez-Ortega, A., Garayo, E. et al. Magnetically activated 3D printable polylactic acid/polycaprolactone/magnetite composites for magnetic induction heating generation. Adv Compos Hybrid Mater 2023, 6, 102. https://doi.org/10.1007/s42114-023-00687-4
33. Kanidi, M.; Loura, N.; Frengkou, A.; Milickovic, T.K.; Trompeta, A.-F.; Charitidis, C. Inductive Thermal Effect on Thermoplastic Nanocomposites with Magnetic Nanoparticles for Induced-Healing, Bonding and Debonding On-Demand Applications. J. Compos. Sci. 2023, 7, 74. https://doi.org/10.3390/jcs7020074
34. Digital method for imprOved Manufacturing of next-generation MultIfuNctIOnal airframe parts H2020 DOMMINIO project (G.A. No. 101007022) https://doi.org/10.3030/101007022
35. Lundström F., Frogner K., Andersson M., Numerical modelling of CFRP induction heating using temperature-dependent material properties, Composites Part B: Engineering, 2021 (220):108982, https://doi.org/10.1016/j.compositesb.2021.108982.
36. Griffiths P., Coativy G., Dalmas F., Falco G., Jiang L., Xiang Z., Le M-Q, Ducharne B., Le Roy D., Méchin F., Bernard J., Meille S., and P. Baeza G.P., Ultrafast Remote Healing of Magneto-Responsive Thermoplastic Elastomer-Based Nanocomposites, Macromolecules 2022 55 (3), 831-843 https://doi.org/10.1021/acs.macromol.1c02046
37. Bermúdez, A., Gómez, D., Muñiz, M.C. et al. Transient numerical simulation of a thermoelectrical problem in cylindrical induction heating furnaces. Adv Comput Math 26, 39–62 (2007). https://doi.org/10.1007/s10444-005-7470-9
38. Díaz-García Á., Law J.Y., Cota A., Bellido-Correa A., Ramírez-Rico J., Schäfer, V. Franco R., Novel procedure for laboratory scale production of composite functional filaments for additive manufacturing, Materials Today Communications, 2020 (24):101049, https://doi.org/10.1016/j.mtcomm.2020.101049.
39. Choupin T., Fayolle B., Régnier G., Paris C., Cinquin J., Brulé B., Macromolecular modifications of poly(etherketoneketone) (PEKK) copolymer at the melting state, Polymer Degradation and Stability, 2018 (155):103-110, https://doi.org/10.1016/j.polymdegradstab.2018.07.005.
40. Kunc, Vlastimil, Kishore, Vidya, Chen, Xun, Ajinjeru, Christine, Duty, Chad, & Hassen, Ahmed A. High performance poly(etherketoneketone) (PEKK) composite parts fabricated using Big Area Additive Manufacturing (BAAM) processes, U.S. Department of Energy Office of Scientific and Technical Information Technical Report, 2016 United States. https://doi.org/10.2172/1343535
41. Martin, R.G., Johansson, C., Tavares, J.R. and Dubé, M. (2022), Material Selection Methodology for an Induction Welding Magnetic Susceptor Based on Hysteresis Losses. Adv. Eng. Mater., 24: 2100877. https://doi.org/10.1002/adem.202100877